Title
Vortical and Internal Wave Shear and Strain

Author
Pinkel, Robert

Vortical and Internal Wave Shear and Strain

ROBERT PINKEL

Scripps Institution of Oceanography, La Jolla, California

ABSTRACT

Depth–time records of isopycnal vertical strain have been collected from intensive CTD profiling programs on the research platform (R/P) *Floating Instrument Platform* (*FLIP*). The associated vertical wavenumber frequency spectrum of strain, when viewed in an isopycnal-following frame, displays a clear spectral gap at low vertical wavenumber, separating the quasigeostrophic (vortical) strain field and the superinertial internal wave continuum. This gap enables both model and linear-filter-based methods for separating the submesoscale and internal wave strain fields. These fields are examined independently in six field programs spanning the period 1983–2002. Vortical and internal wave strain variances are often comparable in the upper thermocline, of order 0.2. However, vortical strain tends to decrease with increasing depth (decreasing buoyancy frequency $N^2 = -g/\rho(d\rho/dz)$ as $\sim(N^2)^{1/2}$, while internal wave strain variance increases as $\sim(N^2)^{-1/2}$, exceeding vortical variance by a factor of 5–10 at depths below 500 m.

In contrast to strain, the low-frequency spectral gap in the shear spectrum is largely obscured by Doppler-smeared near-inertial motions. The vertical wavenumber spectrum of anticyclonic shear exceeds the cyclonic shear and strain spectra at all scales greater than 10 m. The frequency spectrum of anticyclonic shear exceeds that of both cyclonic shear and strain to frequencies of 0.5 cph, emphasizing the importance of lateral Doppler shifting of near-inertial shear.

The limited Doppler shifting of the vortical strain field implies surprisingly small submesoscale aspect ratios: $k_H/k_z \sim 0.001$, Burger numbers Br $= k_H N/k_z f \sim 0.1$. Submesoscale potential vorticity is dominated by vertical straining rather than the vertical component of relative vorticity. The inferred rms fluctuation of fluid vorticity is far less for the vortical field than for the internal wavefield.

1. Introduction

The thermocline is continuously deformed by the passage of internal waves and quasigeostrophic (vortical) motions. This deformation affects the propagation of sound and the spatial distribution of planktonic communities. It renders difficult the interpretation of data. A brief historical discussion of this problem is presented in appendix A. To model these effects it is necessary to separate the vortical and internal wave constituents, as these fields have fundamentally different temporal behavior even though they occupy the same range of spatial scales (Fig. 1). This has proven challenging, experimentally, because lateral and vertical Doppler shifting cause extensive overlap in temporal scales (e.g., Holloway 1983), ostensibly frustrating any attempt to separate the data using a simple frequency filter.

Distinguishing wave and vortical variance is of value in that strain variance estimates are now being used to predict levels of oceanic diapycnal diffusivity (Kunze et al. 2006; Whalen et al. 2012). The assumption is that 100% of the measured strain variance is associated with internal waves, whose breaking drives the mixing. If a substantial fraction of the strain signal is quasigeostrophic, the interpretation of these estimates is in doubt.

Isolating the vortical and internal wavefields is also of value in that the internal wave strain signal is insensitive to purely inertial motions. To the extent that the frequency spectrum of *shear* is dominated by Doppler-shifted inertial waves (Kunze et. al. 1990; Sherman and Pinkel 1991; Pinkel 2008), the frequency spectrum of internal wave *strain* should represent a Doppler-smeared version of the ''underlying spectral continuum.'' If the (normalized) shear spectrum exceeds that which would be predicted from the observed strain, the presence of Doppler-shifted near-inertial shear can be identified.

The problem can be framed in terms of the potential vorticity (PV):

Corresponding author address: Robert Pinkel, Scripps Institution of Oceanography, 9500 Gillman Drive, La Jolla, CA 92093-0213.
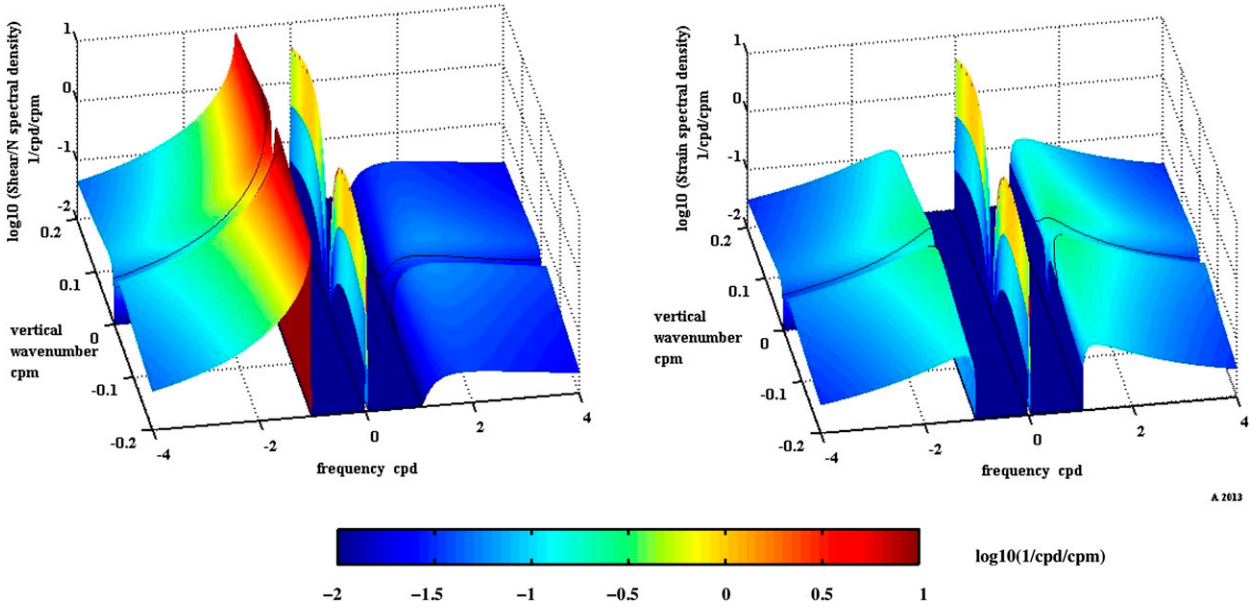E-mail: rpinkel@ucsd.edu

FIG. 1. Schematic vertical wavenumber–frequency spectra of (left) shear/N and (right) strain showing internal wave, $|\sigma| > f$, and vortical $\sigma = 0$ contributions. The axes are chosen to emphasize small vertical scales and near-inertial frequencies. Diagonally opposite quadrants of the spectrum are associated with upward and downward phase velocity. The internal wave spectrum is based on the vertically symmetric Munk (1981) model with parameter $j_* = 40$, to exaggerate the dip in the spectrum at zero wavenumber. The vortical spectrum at $\sigma = 0$ is symmetric in vertical wavenumber. It is otherwise arbitrary in shape and level. The black curves bound that portion of the internal wave spectral domain associated with horizontal phase speeds greater than $0.1\,\mathrm{m\,s}^{-1}$, for an assumed buoyancy frequency of 3 cph. Waves falling outside the bounded region, the Munk (1981) "compliant waves," are presumably strongly advected by the orbital velocity of the faster moving "intrinsic waves," as well as by each other. Spectra such as these would only be observable in an environment where each spectral constituent propagates independently of the variance of signals in other spectral bands. The open ocean poorly approximates this ideal.

$$\Pi = (2\boldsymbol{\Omega} + \boldsymbol{\nabla} \times \overline{\mathbf{V}}) \cdot \boldsymbol{\nabla} B, \tag{1}$$

where $\boldsymbol{\Omega}$ is the vector angular rotation of the earth, $\overline{\mathbf{V}}$ is the fluid velocity, and $B = -g\rho(\mathbf{X}, t)/\rho_0$ gives the fluid density field. Following a fluid parcel, potential vorticity is constant in the absence of nonadiabatic processes (Ertel 1942). Furthermore, propagating internal gravity waves do not induce fluctuations in potential vorticity (Holloway 1983; Muller 1984), whereas finite potential vorticity anomalies are anticipated for quasigeostrophic flows.

The implications of these statements are most easily explored when potential vorticity is linearized assuming horizontal gradients of vertical velocity and buoyancy are small:

$$\Pi = (f + \zeta)N^2(z, t). \tag{2}$$

Here, $\zeta = v_x - u_y$ is the vertical component of fluid vorticity. Further linearizing to neglect the product of vorticity and density perturbations yields

$$\Pi = \overline{N^2}(z)\{f/[1 + \hat{\gamma}(z, t)] + \zeta\} \tag{3}$$

where $\hat{\gamma}$ is the vertical component of isopycnal strain. For convenience in subsequent discussions, an additional

"small strain" assumption is made, and potential vorticity is normalized by $\overline{N^2}$ so as to have units of vorticity:

$$PV = \Pi/\overline{N^2} \sim f[1 - \hat{\gamma}(z, t)] + \zeta \tag{4}$$

For internal waves, the strain and vorticity fields vary in concert such that PV has uniform value f. Thus, the spectrum of strain $E(k)$ directly gives the spectrum of vertical vorticity normalized by f. For quasigeostrophic motions, Muller et al. (1988) [Eq. (A9)] show that the relative magnitude of the ratio of rms vorticity to strain varies as Br^2, where $\mathrm{Br} = k_H N / k_z f$ is the Burger number and k_H, k_z are the horizontal and vertical wavenumbers of the flow constituent. The spectrum of PV is given by

$$PV(k) = (\mathrm{Br}^2 + 1)^2 f^2 E(k). \tag{5}$$

Here, the Burger number gives the contribution to PV from the vertical component of relative vorticity and $E(k)$ is the wavenumber spectrum of vortical strain. Given the difficulty in making direct measurements of oceanic vorticity, obtaining accurate estimates of the flow aspect ratio Br is critical to determining the

relative importance of the rotational versus straining contributions to PV.

Notable observational attacks on this problem include the pioneering work of Muller et al. (1988), who attempted direct estimation of the vertical component of vorticity using current meters from the 1972 Internal Wave Experiment (IWEX) (Briscoe 1975). Kunze et al. (1990) examined shear and strain fluctuations in a weeklong record from a neutrally buoyant float. They found that the dominant departures from linear internal wave theory could be explained by the Doppler shifting of near-inertial shear signals to higher frequencies and high-frequency wave strain signals to lower frequencies. The principal aspect ratios Kunze encountered were of the order $k_H/k_z = 10^{-3}$, with Burger numbers Br ~ 0.1. These were consistent with the earlier towed measurements of Marmorino et al. (1987). Kunze et al. (1990) ascribed the small aspect ratios to the dominance of near-inertial motions, particularly in their shear signal. Subsequently, Kunze and Sanford (1993) attempted direct measurements of strain and relative vorticity using expendable current profilers near Ampere Seamount in the eastern North Atlantic. With two independent profiles of vorticity and strain, they found evidence of submesoscale PV at vertical scales of 50–380 m. Rotational contributions were weaker than those due to strain, but they served to enhance rather than reduce the overall PV, consistent with quasigeostrophic flows. Kunze and Sanford suggested that the PV anomalies were most likely created at the seamount. More recently, Polzin et al. (2003) modeled a vertical wavenumber spectrum of the vortical field. The high-wavenumber dependence of the model was chosen to be consistent with observed correlations of shear and strain, as seen in a large collection of independent vertical profiles obtained in the 1992 North Atlantic Tracer Release Experiment (NATRE) in the subtropical Atlantic. The low-wavenumber portion of the spectral model was constrained by frequency spectra of shear and strain from a nearby mooring. A band-limited form for the vortical spectrum was inferred, with peak variance at vertical scales 7–20 m, and a k_z^{-2} decay at high wavenumber. Polzin et al. suggested that the aspect ratio of the vortical field is $O(10^{-2})$ with Burger numbers Br ~ 1.6.

Attempts to measure the joint depth–time variability of the upper ocean began on the research platform (R/P) *Floating Instrument Platform* (*FLIP*), in 1969. Initially, temperature sensors were rapidly profiled in the vertical, with the upper 400 m of the ocean sampled every 2 min, (Pinkel 1975). CTDs were subsequently introduced and the vertical profiling range was extended [to 800 m in the Hawaii Ocean Mixing Experiment (HOME) Farfield

Experiment] at the expense of the repetition rate. The vertical resolution in density is of the order of 2 m using a SeaBird 911 CTD falling at $\sim 4\,\mathrm{m\,s^{-1}}$. Doppler sonar (Pinkel 1979, 1981) was developed to provide complementary depth–time profiles of velocity. Over the years, sonar vertical resolution was improved to ~ 4 m, adequate for comparing with concurrent measurements of strain.

With measurements continuous in depth and time, time evolution can be tracked in an isopycnal-following [so-called semi-Lagrangian (s-L)] reference frame, avoiding the problem of fine structure contamination due to vertical Doppler shifting. Lateral Doppler shifting, however, remains an issue, and the advection of the short shear and strain-containing motions by the larger-scale energy-containing motions sets the form of the joint wavenumber–frequency spectrum (Sherman and Pinkel 1991, Pinkel 2008) at small vertical scales.

It was initially felt that Doppler smearing would prohibit any frequency-based separation of the vortical and internal wave signals, even in an s-L frame. For example, given Br ~ 1, a 10-m vertical-scale feature is Doppler shifted to frequencies $O(\pm 8 \text{ cpd})$ by a $0.1\,\mathrm{m\,s^{-1}}$ current. It develops that the Doppler smearing of strain is much less than this. The observed vertical wavenumber–frequency spectrum exhibits a subinertial spectral gap between the internal wave and vortical (near-zero frequency) bands at vertical length scales greater than 20 m. The existence of this gap enables construction of a simple model of the vortical spectrum that predicts spectral levels at smaller scales, where the fields are overlapped in frequency. With somewhat less precision, the gap motivates design of a subjective low-pass filter that attempts to separate the vortical and internal wavefields in the space–time domain. Wavenumber and frequency spectra for the vortical and internal wave constituents can be independently estimated, using both the model-based and linear filter approach.

This work is presented in two sections. First, finescale strain records from a series of six eastern Pacific experiments are examined. The vortical and wave constituents are distinguished, based on a total record of nearly 40 000 CTD profiles. Variance profiles, wavenumber spectra, and frequency spectra are given for the vortical and internal wave constituents. Subsequently, finescale shear is compared to strain using data from the 2001 HOME Farfield Experiment. The shear is composed of vortical, internal wave continuum and inertial constituents. The Doppler shifting of the inertial motions across the subinertial frequency band masks the vortical shear signal, precluding even

TABLE 1. Summary of data collection cruises on the *FLIP*. The rms advecting velocity μ gives the magnitude of the velocity that is used in the Doppler shifting model and subjective filter [Eqs. (7) and (8)] to match the observed Doppler broadening of the vortical field, assuming a Burger number of 0.1 for all cruises.

Expt	Year	Latitude	Longitude	Depth range analyzed (m)	Number of profiles	Record duration (days)	Profile time (min)	μ rms advecting velocity (m s^{-1})	$\langle N^2 \rangle^{1/2}/f$
MILDEX	1983	34.5°– 33.5°N	126°– 127°W	50–300	6680	13.91	3	0.06	118
PATCHEX	1986	34.00°N	127.00°W	81–500	9990	20.81	3	0.03	92
SWAPP	1990	35.00°N	127.00°W	100–250	2690	13.5	6.5	0.06	96
ARL	1998	31.41°N	118.70°W	100–680	3869	10.7	4	0.04	71
HOME Farfield	2001	18.39°N	160.70°W	460–680	6000	16.7	4	0.05 (deep)	95 (deep)
				122–680	8990	25		0.08 (full)	158 (full)
HOME Nearfield	2002	21.75°N	158.50°W	122–680	8990	25	4	0.07	90

an approximate separation of the constituent shear fields.

2. Observations of strain: 1983–2002

Extended CTD depth–time profile records are presented, obtained from the *FLIP* in the course of six experiments. With the exception of the earliest cruise (the MILDEX Experiment, in 1983), *FLIP* is anchored with either a one-, two-, or three-point mooring during data collection. Typically, 3000–10 000 CTD profiles are collected over the course of a cruise. Details of each record are summarized in Table 1. To minimize salinity spiking at high profiling speeds, the time response of the Seabird conductivity cell is matched to that of the temperature sensor, leading to a vertical resolution in density of the order 2 m (Anderson 1992)

It is convenient to describe the distortion of the thermocline in terms of a set of isopycnal surfaces $\{z_i(t)\} = \{z(\rho_i, t)\}$, each separated from its neighboring density surface ρ_{i+1} by some constant $\overline{\Delta z}$ in the temporal mean. The normalized isopycnal separation is $\gamma_{ij}(t) = [z_i(t) - z_j(t)]/\overline{\Delta z}$, and finite difference strain is given by $\hat{\gamma}_{ij}(t) = \gamma_{ij}(t) - 1$. [Note that many authors (e.g., Kunze et al. 1990; Polzin et al. 2003) use fluctuations of a vertical temperature or density gradient as a measure of strain. These gradient fluctuations are proportional to $\gamma_{ij}(t)^{-1}$, the inverse of the present definition.] For the strain study presented next, a mean isopycnal separation of $\overline{\Delta z} = 2$ m is used. When strain is later compared with shear in the HOME Farfield Experiment, a mean separation $\overline{\Delta z} = 4$ m is used, consistent with the resolution of the sonar.

The time evolution of isopycnal separation is free of "fine structure contamination" associated with the vertical advection of density features past an Eulerian sensor. One sees a mix of the intrinsic time evolution of the fields and the effects of lateral advection, which are considerable. A representative 12-h record of strain variability from the 2001 HOME Farfield Experiment is presented in Fig. 2.

Three distinct classes of features are seen in the strain portrait. Most prominent are the deltalike striations that occur at fixed densities (depths in this isopycnal-following display) and persist for large fractions of the record. More subtle are the depth-varying wiggles in the individual profiles that evolve smoothly over time. Finally, there are numerous isolated regions where the profiles are disturbed, varying rapidly in time. We identify the first two classes of variability with vortical and internal wave signals. The disturbed regions result from breaking internal waves (Alford and Pinkel 2001).

Wavenumber–frequency spectra of strain are formed by Fourier transforming the strain records in depth and time (Fig. 3). One expects to find a vortical signal at zero frequency. However, as defined here, the set of isopycnals that are followed have zero mean strain. To unambiguously detect a vortical signal, it has to be Doppler shifted sufficiently off zero frequency (one cycle per 2–4 weeks) that its variance appears in a nonzero frequency band. To minimize the impact of the spectral singularity at zero frequency, the average of the spectral estimates in the first and minus-first Fourier bands is placed in the zero-frequency band at each wavenumber, prior to smoothing in frequency. Spectral estimates are corrected for the finite difference approximation to the vertical derivative involved in the strain estimate, through multiplication by the factor $\pi^2 (k_z/k_{Ny})^2/\{2 - 2\cos[\pi^2(k_z/k_{Ny})^2]\}$, where k_{Ny} is ¼ cpm for the strain spectra presented below, and $k_{Ny} = ⅛$ cpm for the HOME Farfield strain and shear spectra that follow. A modeled measurement noise, corresponding to a 1.2-m rms uncertainty in the measurement of isopycnal depth, is then subtracted from
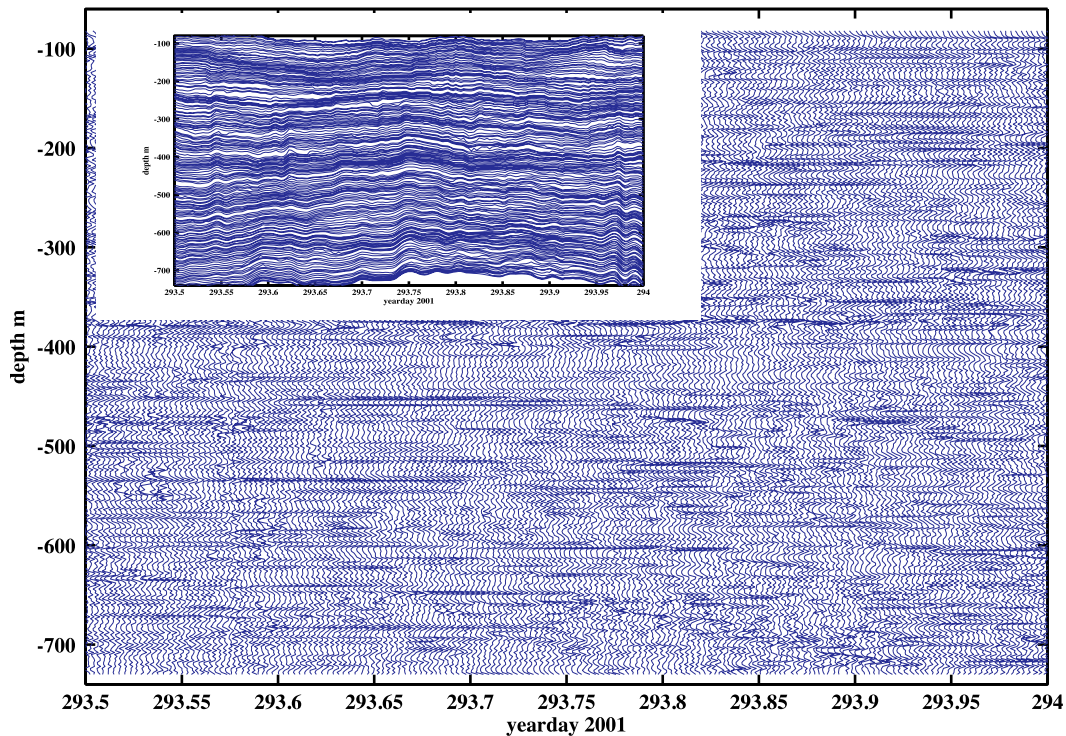
FIG. 2. A 12-h sample of $\log_{10}(\gamma(\overline{z}, t))$, where $\overline{z}$ is the cruise-averaged depth of the isopycnal pair being considered. Isopycnals are separated by 2 m in the vertical, on average, and successive profiles of $\log_{10}(\gamma)$ are plotted at 4-min intervals. Data are from the HOME Farfield Experiment. The inset gives the vertical motion of the isopycnals in physical space over the same time period.

the spectral estimates. This noise, which increases as $|k_z^2|$, can significantly affect the high-wavenumber form of the strain spectrum. Wherever this correction is significant, both corrected and uncorrected versions of the spectrum are presented so that the reader can assess the likely role of measurement imprecision.

In Figs. 3 and 4, the 2-degrees-of-freedom spectral estimates are subsequently smoothed by five bands in frequency and seven bands in wavenumber to produce a nominal 70-degree-of-freedom spectral estimate. In subsequent figures, the smoothing is by five bands in frequency, three in wavenumber, yielding a nominal 30-degree-of-freedom estimate. Diagonally opposite quadrants of the strain spectrum are identical. Positive frequencies and positive wavenumbers correspond to positive/upward phase velocities.

The strain spectrum from the 1986 Patches Experiment (PATCHEX) is representative. It is essentially red in frequency and blue in wavenumber except at the lowest frequencies and wavenumbers: vertical scales greater than 20 m, frequencies less than 2 cpd (Fig. 3, inset; Fig. 4a).

The PATCHEX "vortical ridge," centered at zero frequency, is seen to be band limited in vertical wavenumber, with the greatest variance density at scales

between 10 and 20 m. Two distinct internal wave peaks, associated with upward- and downward-traveling motions of ~40–100-m vertical scale, are seen at slightly superinertial frequency. A semidiurnal tidal strain peak is also seen, centered at zero wavenumber, associated with scales large compared to the 420-m vertical measurement window. At scales smaller than 20 m, the wave and vortical signals merge owing to Doppler smearing, as suggested by Holloway (1983). In terms of wavenumber–frequency spectral density, the vortical peak appears to dominate. However, the wave signal in fact has more total variance, spread over a frequency band that extends to ~100 cpd.

The existence of the spectral gap at low wavenumbers suggests that the vortical and internal wave signals can be separated using either model-based or linear filtering techniques. Pinkel (2008) presents a simple model for the Doppler shifting of an intrinsic spectral line in frequency by random horizontal currents:

$$E_m(\sigma) = E_0/k_H P_V(\sigma/k_H). \qquad (6)$$

Here, E_0 is the variance associated with the spectral line, and P_V is the probability density of the advecting
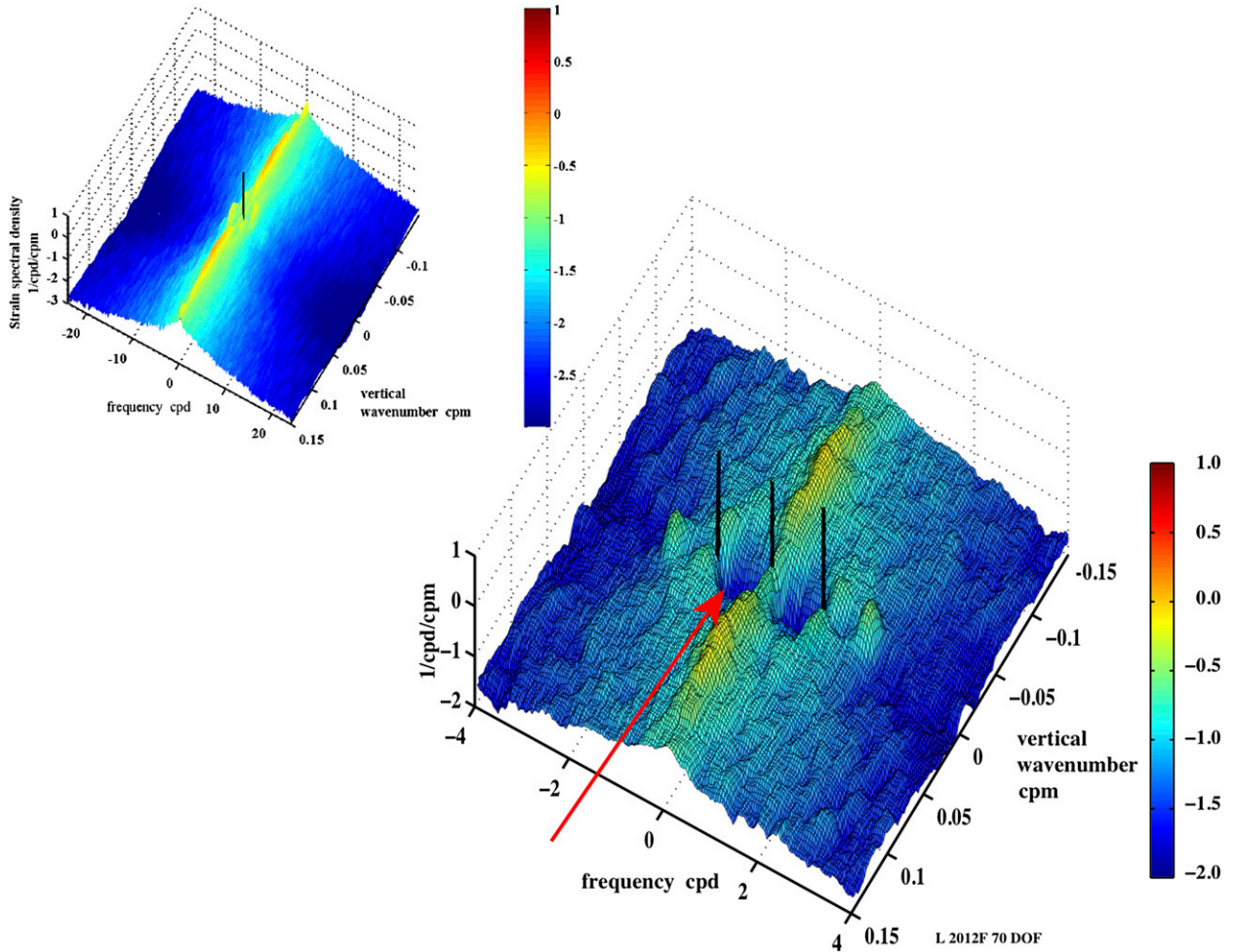
FIG. 3. The wavenumber–frequency spectrum of strain from PATCHEX 1986. The inset shows the spectrum to frequencies of ± 24 cpd. The black vertical reference indicates zero frequency and zero wavenumber. The spectrum assumes an hourglass form. With increasing wavenumber magnitude, spectral variance is Doppler shifted through a broader range of temporal frequencies. The main image gives a closeup of the low-frequency portion of the spectrum, with reference lines at zero wavenumber, $\sigma = 0$, $\pm f$. The arrow indicates the $\sim$15-db spectral gap between the vortical and internal wave bands at vertical scales greater than 20 m. The mirror image of the gap is seen at positive frequencies. This gap is most apparent when time evolution is viewed in a semi-Lagrangian frame and fine structure contamination is not an issue.

horizontal velocity V. By assuming Gaussian P_V and a *fixed* aspect ratio $k_H/k_z = \mathrm{Br}(f/\overline{N})$, the model can be extended across all vertical wavenumbers:

$$E_m(\sigma, k_z) = E_0(k_z)/[\mathrm{Br}(f/\overline{N})k_z]P_V\{\sigma/[\mathrm{Br}(f/\overline{N})k_z]\}. \tag{7}$$

If the model is matched to the observations at the observed frequency $\sigma = 0$, the single adjustable parameter ($\mathrm{Br}\mu$) sets the vortical spectral level at all other frequencies. Here, μ is the rms advecting velocity. An hourglass-shaped spectrum results, with frequency bandwidth increasing linearly with vertical wavenumber. Additional details are given in appendix B.

More ambitiously (and less accurately), one can attempt to separate the vortical and internal wavefields in the depth–time domain. A bandpass filter can be designed, centered on the $\sigma = 0$ vortical ridge in the strain wavenumber–frequency spectrum, with a frequency bandwidth that broadens with increasing wavenumber to account for Doppler shifting. This "subjective filter" has a wavenumber–frequency response in the Fourier domain:

$$W(\sigma, k_z) = W_0 \exp(-\{\sigma/[\sqrt{2}\sigma_w(k_z)]\}^2), \tag{8}$$

where $\sigma_w(k_z) = \mathrm{Br}(f/\overline{N})k_z\mu$, in concert with the analytical model above, and $W_0 = 1$. The filter ideally selects just the vortical constituent, with a frequency passband
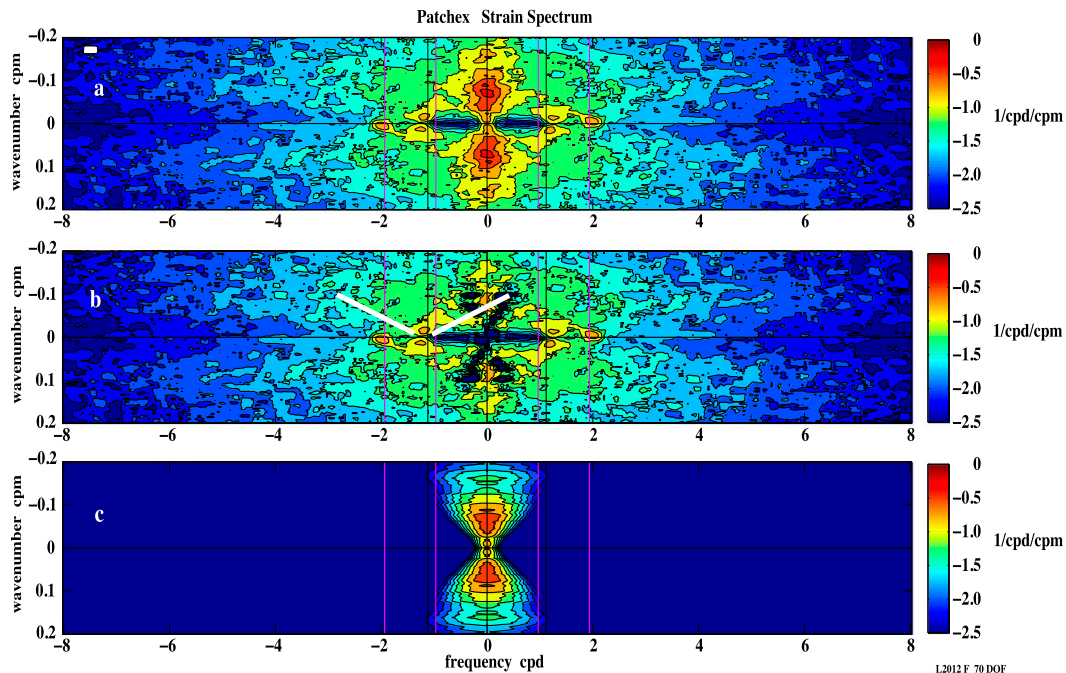
FIG. 4. (a) The PATCHEX vertical wavenumber–frequency spectrum of 2-m strain, as in Fig. 3. Magenta reference lines are drawn at K_1 and M_2 frequencies. Black lines give $\pm f$. The white rectangle indicates the fundamental resolution of the spectrum, corresponding to smoothing by five Fourier bands in frequency and seven in wavenumber. (b) The spectrum of internal wave strain, given as the difference between the total spectrum and the modeled vortical spectrum. White reference lines in (b) schematically indicate the Doppler spreading of superinertial internal wave strain. At like wavenumbers, the wave portion of the spectrum appears more broadly Doppler shifted than the vortical, suggesting a larger aspect ratio k_H/k_z for the wavefield. (c) The modeled vortical spectrum, as described in the text.

that broadens as vertical wavenumber increases. The square root of the filter $W(\sigma, k_z)^{1/2}$ is applied to the two-dimensional grid of strain Fourier coefficients, which are then inverse Fourier transformed back into the depth–time domain. This subjectively filtered vortical strain can be subtracted from the total observed strain field to provide a view of "internal wave strain" in isolation. The subjective filter is nonrealistic in that it accounts for the higher-wavenumber vortical strain being Doppler shifted to progressively higher frequencies, but neglects higher-wavenumber internal wave strain being shifted to progressively lower frequencies into the vortical band.

The PATCHEX strain spectrum, the analytically modeled vortical spectrum, and the residual internal wave spectrum are presented in Fig. 4. The vortical spectral model, Eq. (7), assumes a Gaussian form for the frequency dependence of the spectrum P_V, with a bandwidth increasing linearly with frequency, set by a single adjustable parameter (Brμ).

The quality of this fit is examined in Fig. 5 for all six cruises. Here, frequency cross sections of the strain spectrum are presented at vertical wavenumbers corresponding to 200-, 100-, 50-, and 25-m vertical scales. The

observed, modeled, and residual spectral levels are given in each, with the residual corresponding to the amount of internal wave strain variance Doppler shifted to subinertial frequencies. Given that spectral levels vary over more than an order of magnitude, negative values of the residual are occasionally seen. The key result is that spectral bandwidth indeed appears to increase linearly with the vertical wavenumber. The rate of increase corresponds to surprisingly small (Brμ), $O(\sim 5 \times 10^{-3})$. For reasonable values of rms advecting velocity $\mu = 0.05$–0.1 m s^{-1} (Table 1), the Burger number must be $O(0.1)$ to result in such limited Doppler shifting.

The depth–time domain separation of wave and vortical strain fields produced by the subjective filter is given in Fig. 6. The raw strain field (Fig. 6a) is difficult to decipher, with a mix of wave and vortical motions. In contrast, the internal wave band (Fig. 6b) indeed looks wavelike. Individual wave crests can be tracked for several days as they propagate through the vertical aperture of the array. The upward- and downward-propagating motions correspond to the slightly superinertial spectral peaks seen in Figs. 3, 4a, and 4b. The vortical field (Fig. 6c) evolves slowly with time, reflecting that the subjective filter is
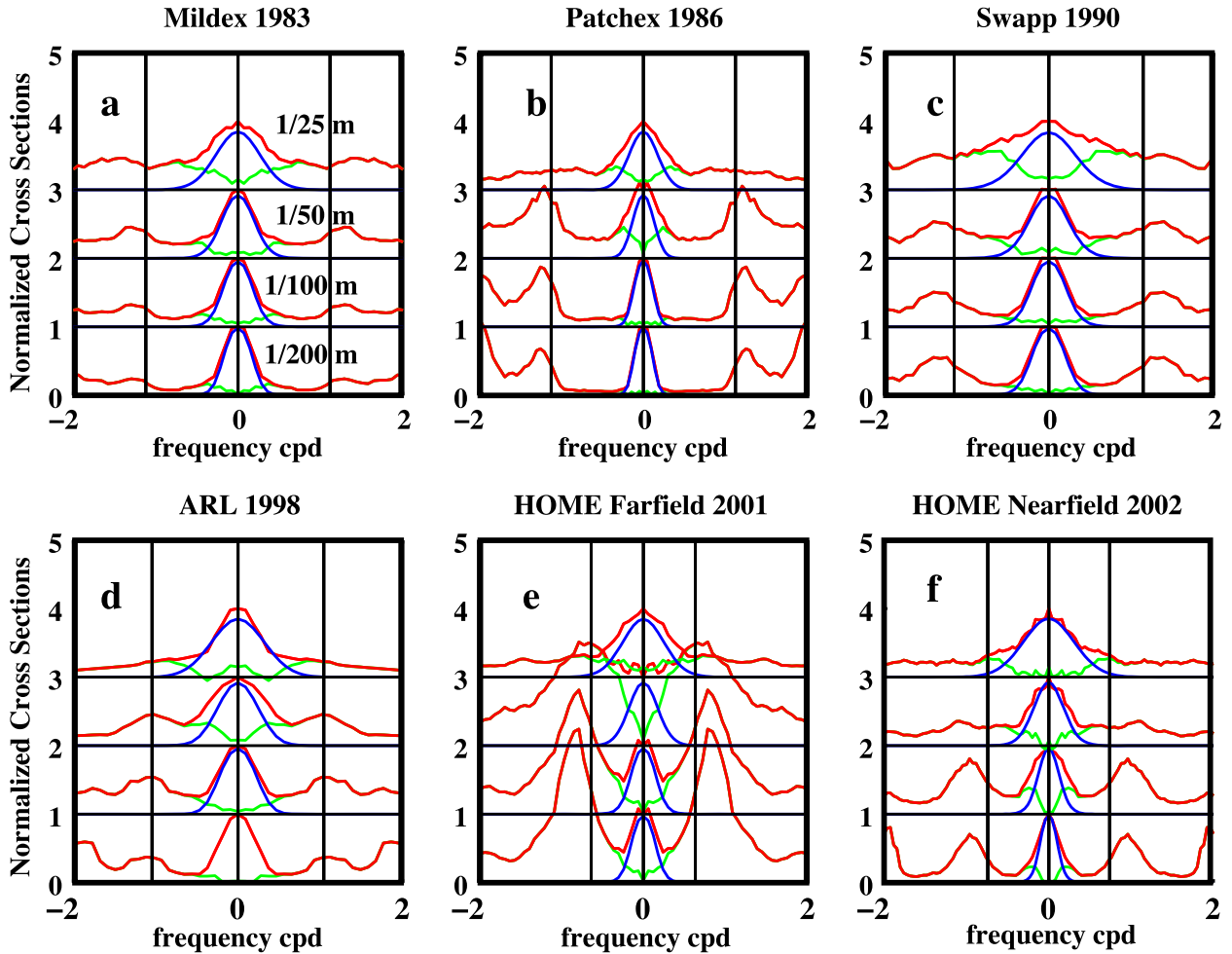
FIG. 5. Model fits (blue) to the observed wavenumber–frequency spectrum of strain (red), at vertical wavenumbers of 0.005, 0.01, 0.02, and 0.04 cpm. The spectra represent the sum of positive and negative wavenumber contributions and are thus symmetric in frequency. Cross sections are normalized to unit height at zero frequency in each wavenumber band. Black vertical lines indicate the local inertial frequency. The green curve is the residual, which ideally represents the amount of internal wave strain that is Doppler shifted into the subinertial band. The product (μBr) is adjusted to fit the model to each of the six cruises. Values for μ are listed in the Table 1, assuming a fixed Br = 0.1.

a form of low-pass filter. However, the features do not tend to wander across density surfaces: long, vertically propagating, crests are not seen. This is a distinct signature of the submesoscale signal.[1]

Profiles of wave and vortical variance as a function of N^2 are presented in Fig. 7. While variance levels in the upper thermocline are somewhat comparable, there is a clear tendency for the vortical variance to decrease with increasing depth, decreasing N^2. The dependence

varies from cruise to cruise between $(N^2)^{1/4}$ and $(N^2)^{1/2}$. In turn, wave strain variance typically grows with increasing depth/decreasing N^2, with dependencies ranging from[2] $(N^2)^{-1/4}$ to $(N^2)^{-1/2}$.

Wavenumber spectra (Fig. 8) are formed by integrating the modeled wavenumber–frequency spectra (Figs. 4b,c) over frequencies less than 24 cpd. Parallel estimates obtained from the subjective filter are also given in Fig. 8. The agreement in estimates calculated by the two differing methods is excellent. The wave strain spectra

---

[1] In fact, a small amount of wandering is seen in the vortical signal. The subjective filter ascribes both vortical and low-frequency high-wavenumber internal wave variance to the "vortical" band. As the filter width is narrowed (the assumed Brμ is reduced), the amount of wandering diminishes.

[2] Recall that the filter overestimates vortical variance at the expense of wave variance, in that the internal wave signal that is shifted to subinertial frequencies is ascribed to the vortical field.
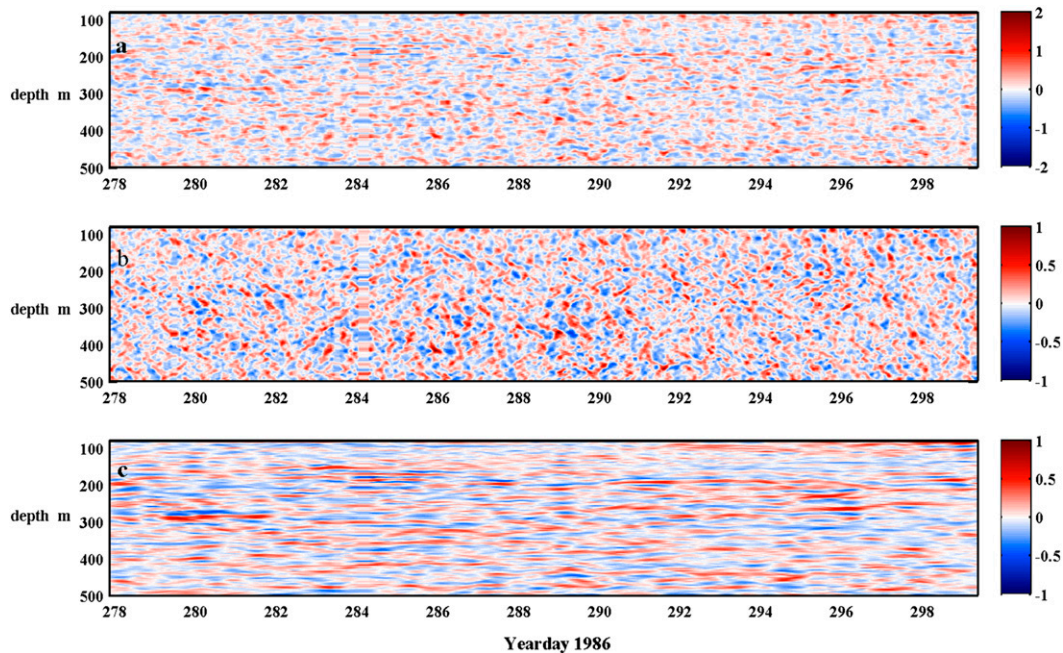
FIG. 6. (a) The complete record of PATCHEX 2-m strain, as in Fig. 2. The data are semi-Lagrangian, with "depth" referring to the average depth of the isopycnal pair involved in the strain calculation. Note the data gap yearday 284–284.5. (b) The subjectively filtered internal wave strain field. Note the change of color scale relative to (a). (c) The subjectively filtered vortical field. Motions constrained to density surfaces appear as horizontal lines in this portrayal.

generally exhibit less cruise-to-cruise variability than the vortical, being whitish at wavenumbers less than 0.03–0.1 cpm and decaying at a higher wavenumber. Vortical wavenumber spectra are uniformly smaller. They are generally band limited, with a broad maximum at the 10–50-m vertical scale. The lower-wavenumber extreme of the vortical spectrum is sensitive to local mesoscale activity. [The Surface Wave Process Program (SWAPP; Fig. 8c) was staged in a frontal region.]

Strain frequency spectra (Fig. 9) are formed by integrating the two-dimensional spectra over all wavenumbers less than $|k_z| = 0.1$ cpm. They are remarkably featureless, with spectral slopes generally less than σ^{-1} at subinertial frequencies and slightly greater at superinertial. The semidiurnal tidal peak is either absent or small, even at principal generation sites such as the HOME Nearfield. The rich structure of tidal harmonics seen in vertical displacement spectra (e.g., Pinkel 1983) is absent in strain, the harmonics being low-mode motions.

Both the model and the subjective filter separate the strain into plausible vortical and wave frequency spectra.

3. Observations of shear and strain: The 2001 HOME Farfield Experiment

During September–November 2001, *FLIP* was moored at 18.39°N 160.7°W, participating in the HOME Farfield Experiment. While the site was in a broad tidal beam emanating from Kaena Ridge, Hawaii, it was over 400 km from the ridge. Baroclinic tidal amplitudes were not unduly large. Bispectral analysis (Sun and Pinkel 2013) indicated that the generation of near-inertial motions by subharmonic energy transfer from the baroclinic tide [parametric subharmonic instability (PSI)] was not significant at the site.

Instrument systems onboard included a pair of profiling CTDS that transited the depth range 5–720 m at 4-min intervals. Shear was measured with the Scripps Institution of Oceanography (SIO) Deep-8 Doppler sonar, which transmitted upward (160 kHz) and downward (140 kHz) from a depth of 360 m. Depth resolution is characterized by a triangular resolution window of half-width (depth) 4 m. Velocity averages are formed over 4-min intervals and stored in 2-m bins. A record of more than 9880 CTD profiles was obtained over a 30-day period of continuous operation (interrupted by occasional equipment malfunctions). An energetic anticyclonic eddy, shed from the Big Island of Hawaii, passed by *FLIP* during the final third of the cruise, clearly affecting shear and strain at depths above 400 m.

In the semi-Lagrangian frame, the finite-difference shear is given by $S_{ij} = [u(\rho_i, t) - u(\rho_j, t)]\gamma_{ij}(t)^{-1}/\overline{\Delta z}$.
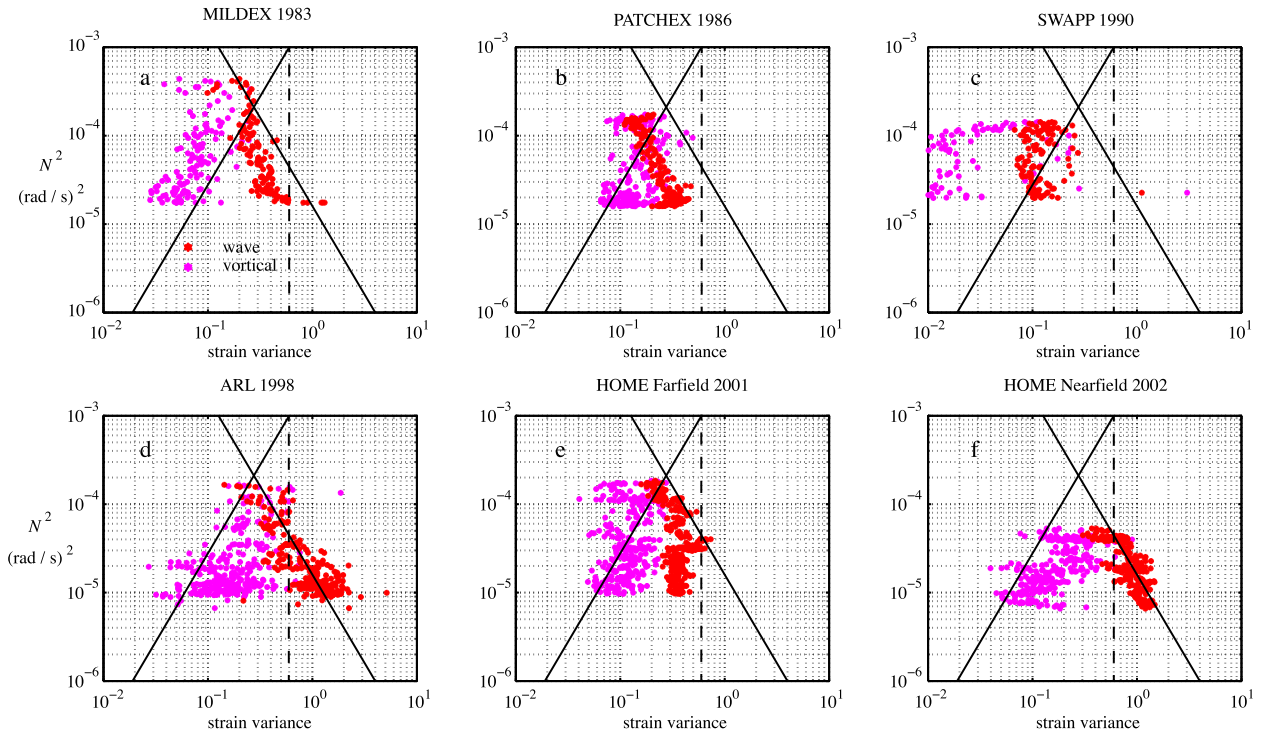
FIG. 7. Profiles of internal wave (red) and vortical (magenta) strain variance vs N^2, obtained by applying the subjective filter to 2D Fourier transforms of strain and then inverse transforming back into the depth–time domain, as in Fig. 6. Reference lines $(N^2)^{1/2}$ and $(N^2)^{-1/2}$ are drawn. Generally, internal wave strain increases with depth/decreasing N^2, while vortical strain decreases.

Here, $u(\rho_i, t)$ is the along-isopycnal (taken here as horizontal) velocity, which is nearly statistically independent of isopycnal separation (Pinkel and Anderson 1997). Shear, with a factor of γ in the denominator, is strongly dependent on strain. For this analysis of the HOME Farfield data, a set of isopycnals $\{\rho_i\}$ is selected such that the mean separation $\overline{\Delta z} = 4$ m is commensurate with the vertical resolution of the Doppler sonar. Shear and strain depth–time series are formed from 100 to 700 m. The shear records are normalized by $\overline{N}(\overline{z}_i)$, the mean buoyancy frequency at the mean depth of each isopycnal surface, following Polzin et al. (2003). The normalized shear $S/\overline{N}(z)$ and strain records are Fourier transformed in depth and time to form vertical wavenumber–frequency spectra. Spectra are weighted by the factor $(2\pi k_z)^2/[2 - 2\cos(\pi k_z/k_{Ny})]$ to account for the finite difference approximation made in forming the shear and strain. Here, $k_{Ny} = \frac{1}{8}$ cpm is the Nyquist wavenumber. The shear spectrum is further divided by the factor $[\sin(\pi k_z/k_{res})/(\pi k_z/k_{res})]^4$, where $k_{res} = \frac{1}{4}$ cpm to account for the finite resolution of the sonar and the subsequent averaging in range of the velocity estimate.

The analysis is, in fact, repeated three times: first using 6000 4-min profiles from 400 to 700 m, from before the arrival of the Big Island Eddy, to produce representative two-dimensional spectral estimates (Figs. 10, 11). The full depth–time record (9880 profiles) is then used for Figs. 12 and 13 to illustrate the influence of the eddy on the strain field. Finally, 1D wavenumber and frequency spectra (Figs. 14, 15) are estimated from the first 6000 profiles, again avoiding eddy influence.

Shear time series are complex with real and imaginary parts corresponding to the east and north components of shear. Thus, the wavenumber–frequency spectrum of shear has four independent quadrants, with anticyclonic rotation (henceforth ACy; cyclonic is Cy) in time for $\sigma < 0$, and anticyclonic rotation with increasing depth for $k_z < 0$. Strain is a real signal, and diagonally opposite quadrants of the strain spectrum are identical. For both shear and strain, upward phase propagation corresponds to $\sigma < 0$, $k_z < 0$, $\sigma > 0$, and $k_z > 0$. Downward phase propagation occurs in the remaining quadrants.

The shear spectrum (Fig. 10, left) peaks strongly at frequency $\sigma = -f$, the local inertial frequency. The
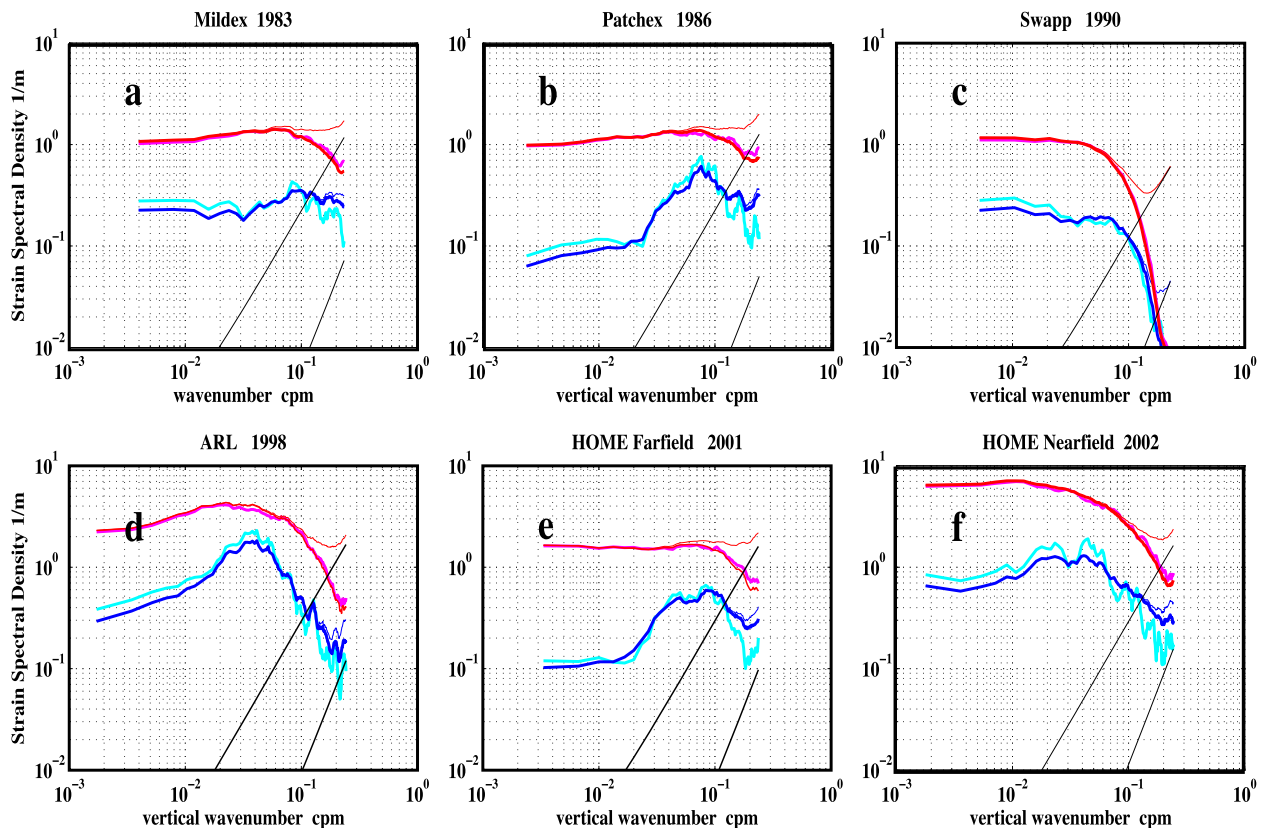
FIG. 8. Wave (red, magenta) and vortical (light/dark blue) wavenumber spectra. The separation is based on either the subjective filter, which assigns 100% of the variance in a prescribed band to the vortical field (dark blue), or to the analytical model, which determines the vortical field from the height of the zero-frequency spectral ridge (light blue). The subjective filtered wave and vortical spectra are shown uncorrected (thin red and dark blue) and corrected (thick red and dark blue) for an assumed 1.2-m rms error in estimating isopycnal depth.

frequency bandwidth of the spectral peak is smallest at low vertical wavenumbers, quickly broadening with increasing wavenumber magnitude until the peak fills the subinertial band $-f < \sigma < 0$ and even spreads into positive frequencies. The inertial peak also spreads broadly into the internal wave band. Using simple models of Doppler shifting, Pinkel (2008) argued that the frequency spectrum of the shear was dominated by the Doppler-smeared inertial peak to frequencies of nearly ± 20 cpd.

In contrast, the spectrum of strain (Fig. 10, right) formally has no inertial peak to be Doppler smeared. The strain spectrum provides a view of the vortical and continuum internal wavefields unobscured by inertial smearing. The spectrum features a strong vortical signal centered on zero frequency, similar to that in PATCHEX (Figs. 3, 4) and other sites. The internal wave continuum peaks at low wavenumber at slightly superinertial frequency. Plan views of the shear and strain spectra are presented in Fig. 11.

Depth–time images of shear and strain are presented in Fig. 12. The normalized zonal shear, $S/\overline{N}(z)$, (Fig. 12a) is dominated by near-inertial motions, Doppler shifted to both super- and subinertial frequencies. The corresponding 4-m strain signal (Fig. 12b) is complicated, marked by horizontal striations that constitute the vortical contribution. When these are removed via the subjective filter, a rich continuum of propagating motions is seen (Fig. 12c). The motions are of characteristically higher frequency than the shear and extend to smaller vertical scales. The vortical strain (Fig. 12d) is a mix of low-frequency eddy activity above 300 m and high vertical wavenumber striations that generally do not cross isopycnal surfaces. The slow time variation of this field is a consequence of the selective filer. Downshifted internal waves leak into this band at a high wavenumber, leading to some traces of vertically propagating signals.

The variance of shear/N, wave, and vortical strain are plotted versus N^2 in Fig. 13. The variance of these 4-m strain estimates is approximately half that of the 2-m strain (Fig. 7e) calculated from the same data. Vortical variance fluctuates irregularly for $N^2 > 3 \times 10^{-5}\,\mathrm{s}^{-2}$ and decreases with decreasing N^2 below. Wave strain
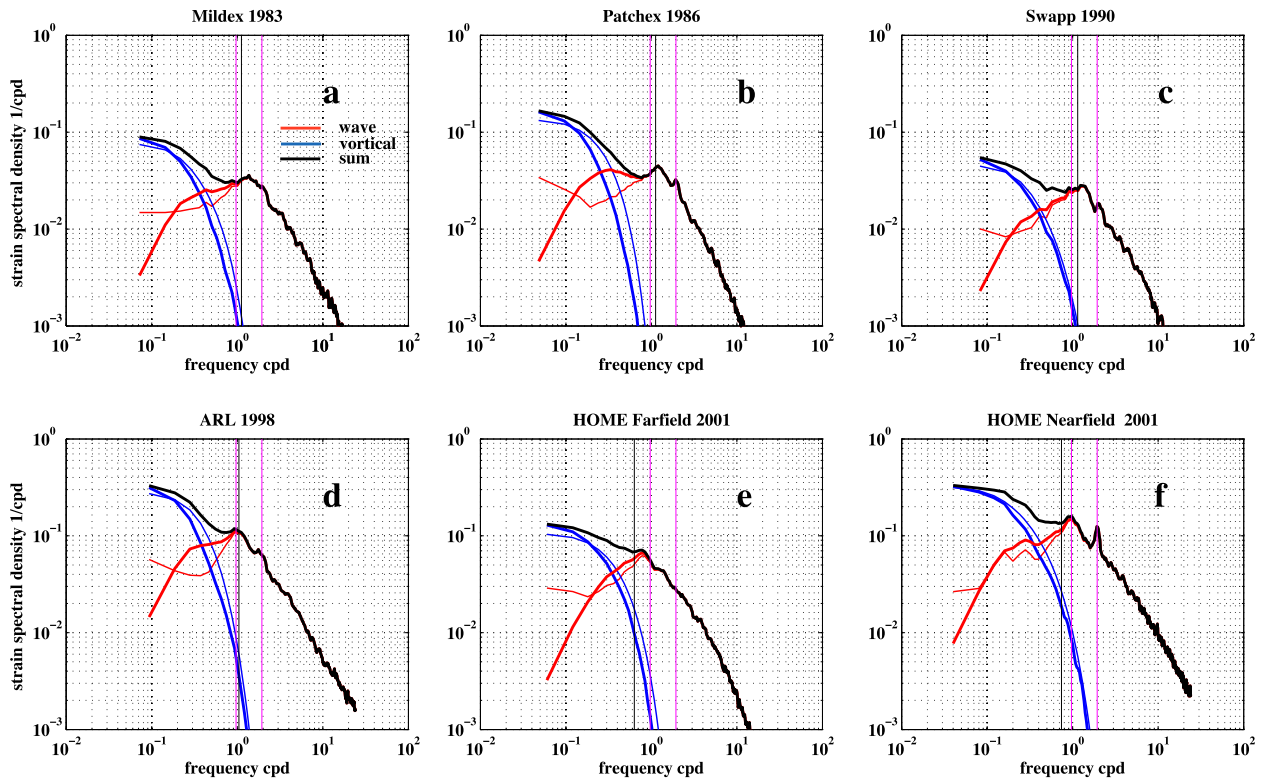
FIG. 9. Frequency spectra of strain (black) separated into wave (red) and vortical (blue) constituents. Thick lines indicate the model separation, while thin lines give the subjective filtered equivalent. Vertical reference lines are drawn at f (black) and diurnal and semidiurnal frequencies (magenta).

variance increases weakly for $N^2 > 3 \times 10^{-5}\,\mathrm{s}^{-2}$, becoming more nearly constant at greater depth. Wave strain variance exceeds vortical strain variance by a factor of 3–5. The $S/\overline{N}(z)$ variance changes by a factor of 3 over the 100–700-m depth range, with a broad maximum at $N^2 \sim 4 \times 10^{-5}\,\mathrm{s}^{-2}$. Normalized shear variance generally exceeds wave strain variance by a factor of 5. This reflects the influence of near-inertial waves, which contribute preferentially to the shear versus strain fields. For the Garrett–Munk (GM) spectral model (Munk 1981), the variance of $S/\overline{N}(z)$ is uniform with depth.

Vertical wavenumber spectra of 4-m shear and strain are estimated from wavenumber–frequency spectra calculated over the depth ranges 100–300 and 460–660 m. These are integrated over frequencies less than 24 cpd. Individual spectra of ACy and Cy $S/\overline{N}(z)$, as well as internal wave and vortical strain, are presented in Fig. 14. Note that here, ACy and Cy refer to the sense of rotation in time, in contrast to the traditional "rotary wavenumber spectrum" of shear, where rotation is considered as a function of depth (Leaman and Sanford 1975). The ACy shear spectrum is dominant, exceeding the Cy shear and strain spectra by a factor of 3–5. It is strongly band limited, peaking at $O(50\mathrm{m})$ scales and

decaying at a high wavenumber with a slope $O(k_z^{-2})$. The Cy spectrum peaks at slightly smaller scales, $O(30\mathrm{m})$, and decays more slowly at a high wavenumber, eventually joining the ACy at ~10-m vertical scales. Much of the Cy variance results from ACy inertial motions that are Doppler shifted across the ACy–Cy boundary (Fig. 10, left). The dominance of the ACy spectrum reflects the importance of inertial motions in determining the overall shear field in the sea.

Even though N has decreased by a factor of 2 between the upper and lower depth ranges, there is no corresponding shift of the $S/\overline{N}(z)$ spectrum to smaller vertical wavenumber. The implication is that the shear-containing waves in the upper depth range do not freely propagate to the lower depth range under Wentzel–Kramers–Brillouin (WKB)-like refraction. Rather, local equilibrium processes set the form of the shear spectrum at each depth.[3]

---

[3] The specific near-inertial wave groups propagating through the upper depth range will have traveled tens to hundreds of kilometers laterally before reaching the depth range of the lower spectrum.
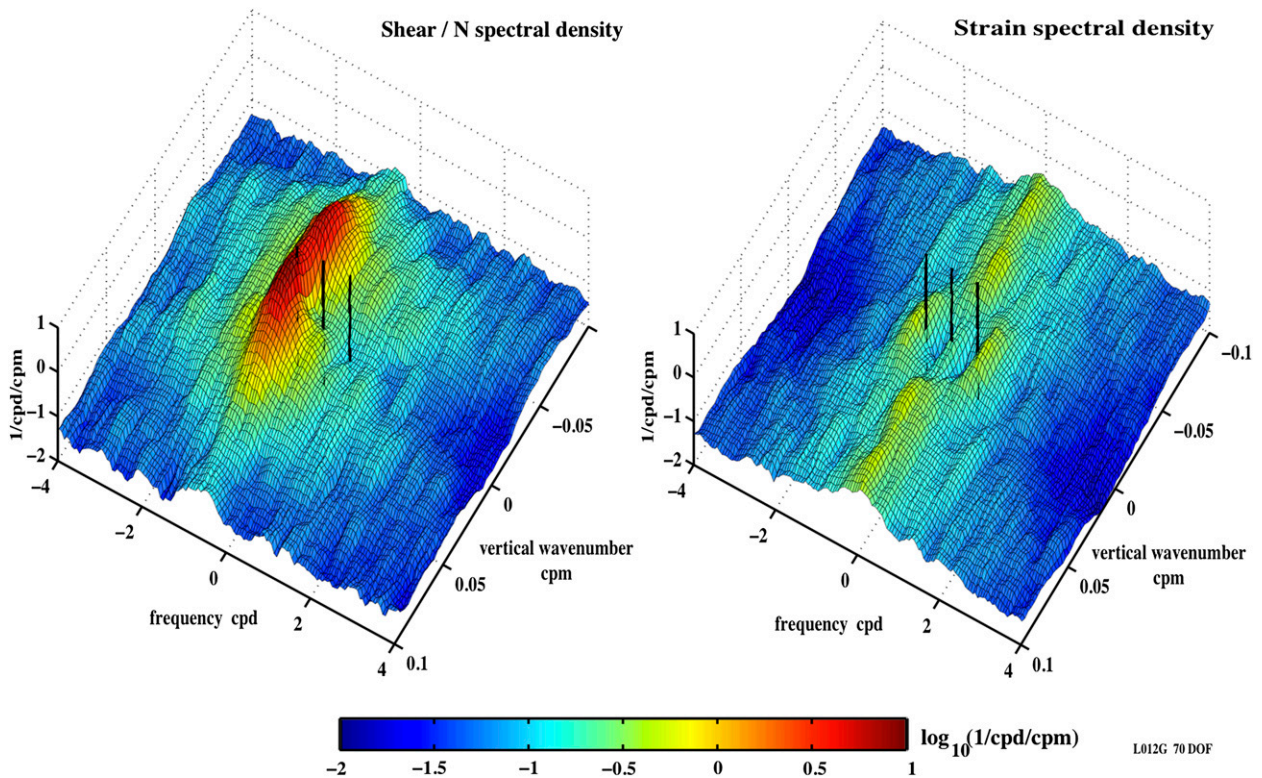
FIG. 10. Spectra of (left) $S/\overline{N}(z)$ and (right) strain from the HOME Farfield Experiment 2001. Data are from 460–660 m from the first 16.7 days of the experiment, avoiding the influence of an energetic eddy. The black vertical references indicate zero wavenumber at frequencies $(-f, 0, f)$. The spectral gap between wave and vortical fields at low-wavenumber magnitude is apparent in both spectra. At intermediate wavenumbers, the near-inertial shear is Doppler shifted from $-f$ across zero frequency and into the positive (cyclonic) frequency band, completely obscuring any sign of a vortical ridge.

The internal wave strain spectra, when corrected for the finite difference approximation, are essentially white. The low-wavenumber spectral level is comparable to the Cy shear. At $O(30\,\mathrm{m})$ vertical scales, the Cy shear significantly exceeds the wave strain, perhaps due to the Doppler smearing of high-wavenumber near-inertial variance across the $\sigma = 0$ ACy–Cy boundary.

The lack of a high-wavenumber rolloff in the strain spectrum is perhaps associated with measurement noise. When a modeled k_z^{+2} noise spectrum (Fig. 14, black lines) is subtracted from the wave strain, the data begin to exhibit a high k_z rolloff. The level of the noise spectrum corresponds to a precision of 1.2-m rms in identifying the depth of an individual isopycnal surface.

The vortical strain spectrum assumes a band-limited bluish form. The vortical spectrum is a factor of 3–5 smaller than the wave spectrum. A similar noise correction is applied to the vortical wavenumber spectrum as for the wave strain.

Frequency spectra of ACy and Cy $S/\overline{N}(z)$ and vortical and wave strain are presented in Figs. 15a and 15b for the 100–300- and 460–660-m depth ranges. Spectra are averaged in depth and then smoothed in frequency, with incrementally increased smoothing as frequency increases. The ACy shear spectrum peaks at the inertial frequency and decays as $\sim\sigma^{-2}$ to frequencies of 6–10 cpd. Spectral slopes progressively decrease up to a weak cutoff at the buoyancy frequency. The Cy spectra display a variable $\sim\sigma^{-2/3}$ slope at low frequency, merging with the ACy at $\sigma = 8 - 10$ cpd. Both spectra extend into the subinertial band, primarily due to Doppler shifting (Fig. 10, left).

The strain spectrum generally parallels the Cy spectrum at low frequencies. At high frequencies the slope increases, approaching σ^{-2} form at frequencies of about 8–10 cpd. The subjective filter partitions strain variance into vortical and wave spectra. The wave strain spectrum peaks at frequencies around 1 cpd and dominates the strain signal at higher frequencies. For linear internal waves at superinertial frequencies, spectral levels of $S/\overline{N}(z)$ and strain should be identical, that is, the upper black curve and the lower black/red curve in Fig. 15 should merge. Here, they get close, particularly for the deeper data. At low frequency, the prevalence of Doppler-shifted near-inertial shear keeps the ACy
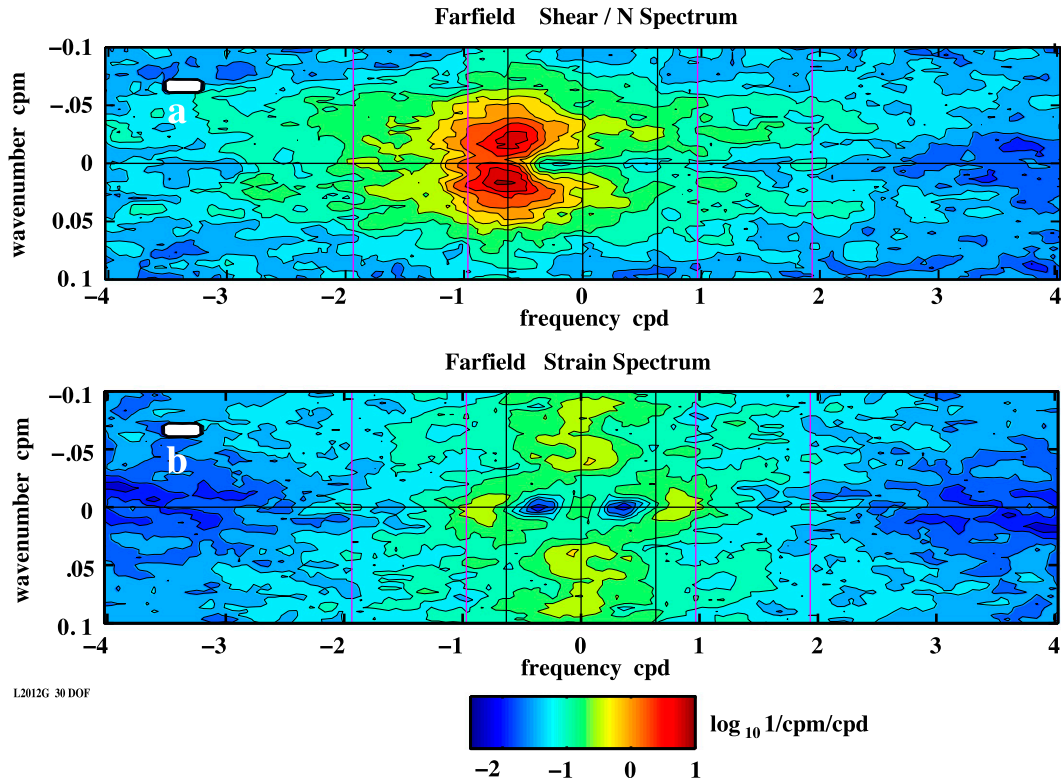
FIG. 11. Vertical wavenumber spectra of (a) $S/\overline{N}(z)$ and (b) strain for the 460–660-m depth range of the HOME Farfield Experiment, as in Fig. 10. Black reference lines indicate frequencies $\pm f$. Magenta lines give frequencies M_2 and K_1. All four quadrants of the shear spectrum are independent, with negative frequencies corresponding to anticyclonic rotation of the shear vector in time. The white rectangle indicates the fundamental resolution of the spectrum, smoothed by five Fourier bands in frequency and three in wavenumber.

$S/\overline{N}(z)$ spectrum well above the strain spectrum. The Cy $S/\overline{N}(z)$ spectrum should be free of near-inertial motions. Indeed, its level is close to (half of) the observed strain spectrum at low frequency. Unfortunately, there is no low-frequency cutoff at the inertial frequency. These Cy motions are contaminated by the Doppler shifting of the ACy near-inertial motions across the $\sigma = 0$ boundary (Figs. 11, 12) and are not a good metric of the super-inertial "internal wave continuum."

For submesoscale motions in the linear limit, the ratio of normalized shear to strain variance is given by Br^2 (Muller et al. 1988). If the vortical Burger number is indeed $O(0.1)$, as here inferred from the *lack* of Doppler shifting seen in the strain wavenumber frequency spectrum, it follows that the submesoscale contribution to the overall shear field in the sea is negligible (Fig. 15, dotted magenta line).

4. Discussion

The essential observation here is that the lateral Doppler shifting of submesoscale motions is a much smaller effect than originally anticipated. Levels are consistent with flow aspect ratios of $k_H/k_z \sim 10^{-3}$ and Burger numbers $O(0.1)$. The case is summarized in Fig. 4, where the degree of Doppler shifting of the vortical field (Figs. 4a, c) to higher frequencies is clearly less than the Doppler shifting of superinertial internal waves into the subinertial band (Fig. 4b). Given that the aspect ratio of near-inertial internal waves is smaller than f/N, the submesoscale aspect ratio must be still less. The implication is that the predominant source of submesoscale PV fluctuation in the open ocean thermocline is vertical straining, with relative vorticity playing a much smaller role [Eq. (4)].

Given our ability to isolate the submesoscale straining, the normalized rms potential vorticity $PV/f = \langle \gamma_{vort}^2 \rangle^{1/2}(1 + Br^2)$ can be estimated directly (Fig. 16a). In order that internal waves induce no PV fluctuation, wavefield straining must be countered by an associated rms relative vorticity $\zeta_{rms} = f\langle \gamma_{IW}^2 \rangle^{1/2}$. This greatly exceeds the relative vorticity of the sub-mesoscale if Burger numbers are indeed $\ll 1$ (Fig. 16a).

Given an estimate of the vertical wavenumber spectrum of submesoscale strain (Fig. 7), one can
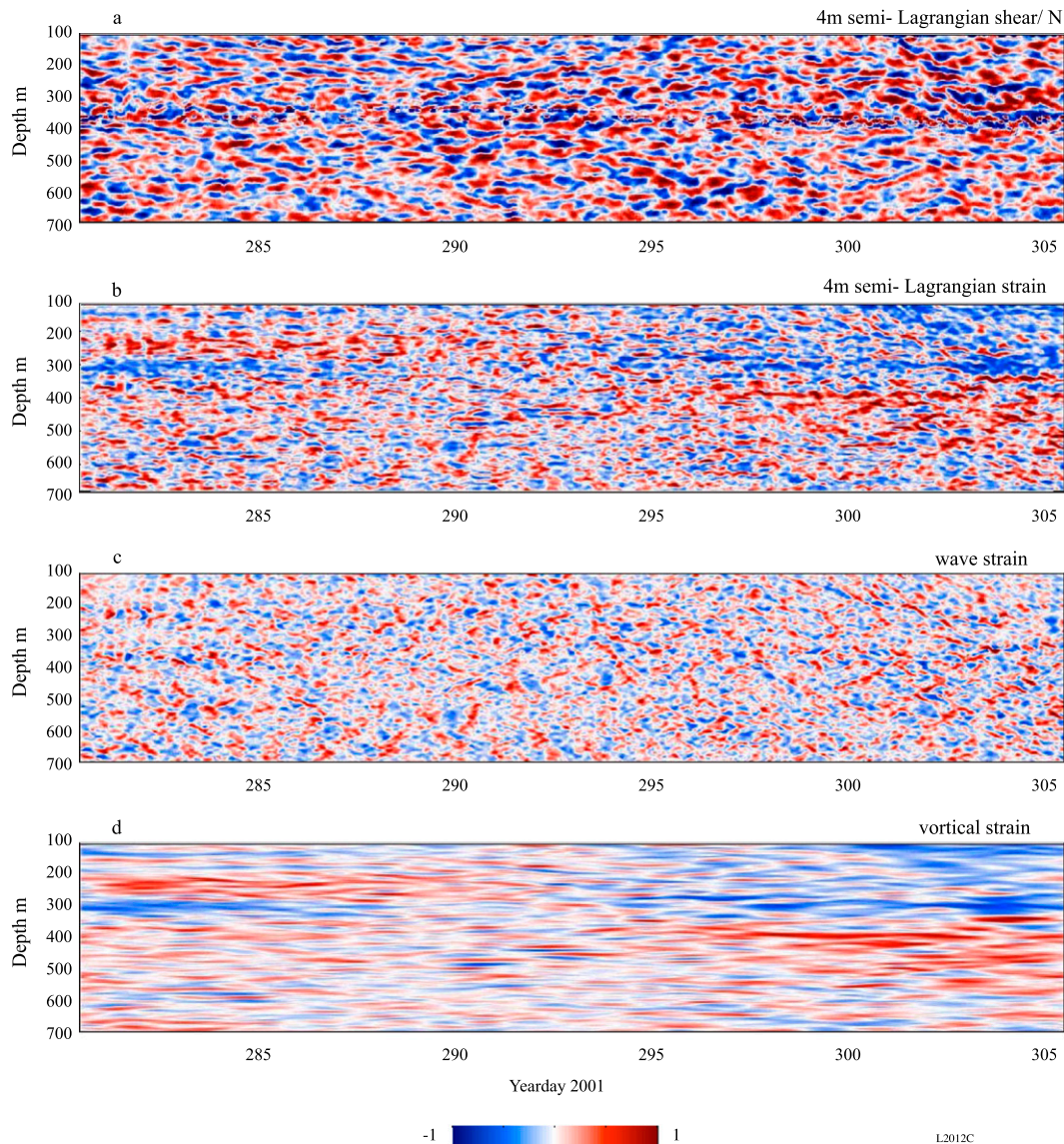
FIG. 12. Depth–time views of (a) the zonal $S/\overline{N}(z)$ field and (b) the total strain field for the HOME Farfield Experiment, presented in semi-Lagrangian coordinates. The strain is further separated into (c) an internal wave constituent and (d) a vortical field using the subjective filter. The passage of a Big Island Eddy is seen in the general compression of isopycnals (negative strain, blue) in the upper 300 m following yearday 300.

produce a corresponding spectrum of potential vorticity fluctuation as a function of horizontal wavenumber magnitude (Fig. 16b). This can be compared with both towed observations and with contemporary numerical simulations of submesoscale flow. Critical to the conversion is a knowledge of the aspect ratio of the flow. As Burger numbers increase (from an assumed lower limit of 0.1 here), the spectrum shifts to a higher horizontal wavenumber magnitude, its wavenumber bandwidth increases proportionally, and the assumed contribution of relative vorticity to the overall PV field

increases as Br^4. Given the magnitude of the observed rms vortical strain, predicted rms relative vorticity exceeds f for $Br > 2$.

The vortical wavenumber spectrum (Figs. 7, 16b) is typically band limited, with maximum variance concentrated between 10- and 50-m vertical scales. Polzin et al. (2003) also infer a band-limited form from their study of vertical shear and strain profiles. Most modelers anticipate a red spectrum for the mesoscale/submesoscale density field as a function of horizontal wavenumber. Perhaps this distinct submesoscale
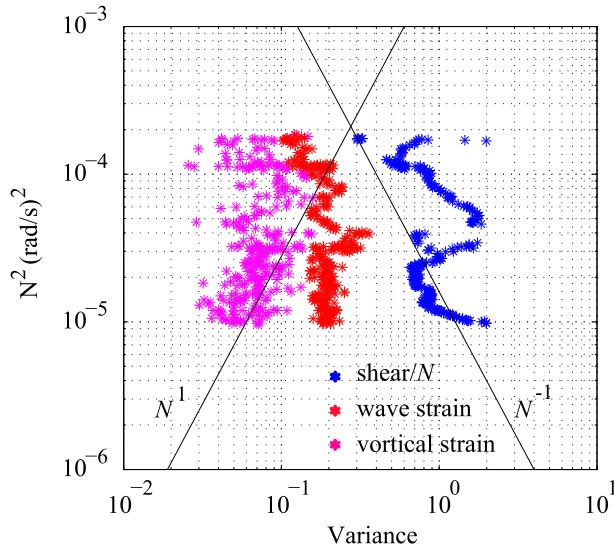
FIG. 13. Variance of $S/\overline{N}(z)$, internal wave, and vortical strain from the HOME Farfield Experiment.

signature exists as a high-wavenumber spectral shoulder on an "otherwise red" low-wavenumber spectrum of density. Alternatively, in the present study, *only* motions that are significantly Doppler shifted off "zero frequency" (one cycle per 2–4 weeks) are considered. Lower-frequency motions are deemed background and considered part of the basic state against which fluctuations are defined. To the extent that larger vertical scales are associated with larger horizontal scales and less Doppler shifting, there is an inherent bias against large-scale fluctuations in this work.

The central assertion that submesoscale aspect ratios are $O(10^{-3})$, Br ~ 0.1, is based on the observation that vortical motions seem to be Doppler shifted much less than for internal waves of corresponding vertical scale. Implicit in this thinking is that the orientation of lateral gradients induced by both waves and vortical flows is random with respect to the advecting currents. If density gradients are not random in direction, but aligned normal to the direction of the advecting current, as is the case for geostrophic flow, there will be no Doppler shifting. This must be a factor at the largest scales. But one envisions the smaller-scale vortical field to be embedded in the larger-scale flow and more or less passively advected. Perhaps submesoscale lateral gradients are aligned by the straining of the larger-scale flows. If so, the large-scale strain and velocity fields must also be aligned for this effect to be significant.

To quantify the degree of alignment required, the random Doppler-shifting model of Pinkel (2008) [Eq. (6),

appendix B here] is modified to account for anisotropy in appendix C. When "crest orientation" is allowed to vary randomly within $\pm \Delta \theta$ degrees of the direction of the advecting velocity and the advecting velocity magnitude is varied with a Rayleigh probability distribution, the resulting Doppler spectrum is more peaked and concentrated than a Gaussian. For fixed rms advecting velocity μ, the spectrum both broadens and approaches a Gaussian form as $\Delta \theta$ is increased from small values toward $\Delta \theta = \pi/2$.

To reduce Doppler shifting by a factor of 10, corresponding to vortical aspect ratios of 10^{-2}, Br ~ 1, one needs to have submesoscale lateral gradients normal to the advecting flow direction to within $\Delta \theta = \pm 10°$ (Fig. C1). While this is not out of the realm of possibility, it must occur in an environment where small-scale internal waves, themselves effectively passively advected by the larger-scale currents, are not also aligned by the large-scale strain field.

5. Summary

Repeated profiles of horizontal velocity and density are used to form wavenumber–frequency spectra of shear and strain in an isopycnal-following frame. For the strain spectra, there is a distinct spectral gap at low wavenumber (vertical scales > 20 m) between the inertial frequency and zero frequency. The existence of this gap suggests both modeling and linear-filtering approaches to enable a separation of the vortical (intrinsically subinertial) and internal wave (intrinsically superinertial) fields.

The internal wave strain frequency spectrum is surprisingly featureless, peaking at slightly superinertial frequencies with a hint of an M_2 tidal peak only in regions of strong tidal generation (Fig. 9). This spectrum is presumably a Doppler-shifted version of "the internal wave continuum," in the absence of Doppler-smeared near-inertial motions. Not surprisingly, the semi-Lagrangian shear/N spectrum is far greater than the strain in the near-inertial and low-frequency bands. Oddly, the shear/N spectrum is also greater than the strain at *high* encounter frequency (Fig. 15). To the extent that the shear to strain ratio is a measure of intrinsic wave frequency, the suggestion is that even high-frequency shear is intrinsically near inertial.

This near-inertial dominance is also seen in the vertical wavenumber spectra of Cy and ACy shear/N (Fig. 14). Here, Cy and ACy refer to the sense of shear rotation in *time*, not depth. The ACy shear greatly exceeds the Cy shear at all scales greater than 10 m, again indicating the presence of inertial motions.
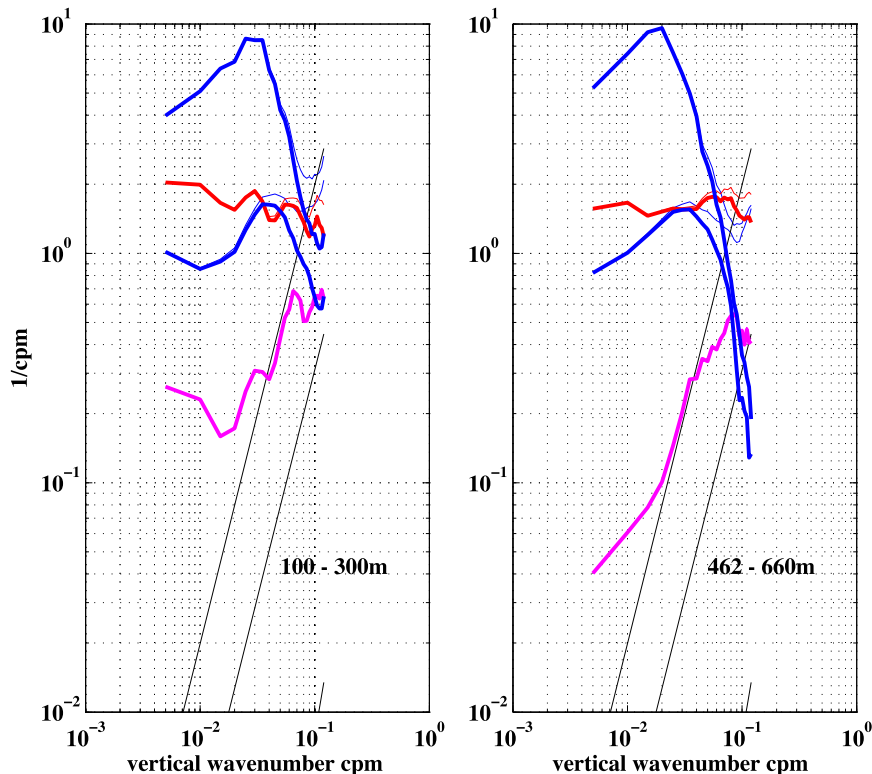
FIG. 14. Vertical wavenumber spectra of $S/\overline{N}(z)$ and strain from (left) 100 to 300 m and (right) 462 to 660 m. The upper blue line is the anticyclonic $S/\overline{N}(z)$, while the lower blue line is the cyclonic constituent. The thick lines reflect subtraction of a modeled noise equivalent to 0.01 m s^{-1} in horizontal velocity, while the thin blue lines give the uncorrected data. The red lines give the internal wave strain spectrum, uncorrected (thin line) and corrected (thick line) for an assumed 1.2-m rms error in estimating isopycnal depth. The magenta curves are the vortical spectrum, as determined by the subjective filter. Wave strain exceeds vortical strain by a factor of 3–5 at vertical scales >20 m. Thin black lines give the modeled noise contribution to the $S/\overline{N}(z)$, wave, and vortical strain spectra.

If inertial shear is Doppler shifted through much of the internal wave frequency band, why are the internal tidal lines and their harmonics so sharp in frequency? There are two contributing answers. First, in regions where tidal generation occurs at supercritical topography, only the lowest modes can escape from the generation site, owing to the intensity of nonlinear processes in the generation region. The low modes have large horizontal scales and are minimally affected by variations in ambient current. Thus, velocity and displacement spectra have sharp tidal peaks, while shear and strain have but weak tidal signatures in the farfield of topographic sources.

There is a second effect associated with generation mechanisms. Inertial waves are generated in an already moving fluid (the mixed layer) by moving phenomena such as storms. When viewed in an Eulerian frame, they are Doppler shifted through a broad range of frequencies. The tidal peaks are, in contrast, principally generated by flow over fixed seafloor topography. When viewed in an Eulerian frame (e.g., by moored measurements), such motions are not Doppler shifted in frequency by *steady* background flows [see Gerkema et al. (2013) for a review]. *Travel time*, rather than frequency, is affected by steady flow (e.g., Rainville and Pinkel 2006). Thus, the various tidal peaks and their harmonics are not Doppler smeared when viewed in an Eulerian frame, while the inertial peak is.

The subjective separation between wave and vortical strain enables separate vertical profiles of variance to be calculated. While wave and vortical variance can be comparable in the upper ocean, vortical variance tends to decrease with depth as $(N^2)^{1/4}$–$(N^2)^{1/2}$, while wave strain variance increases as $(N^2)^{-1/4}$–$(N^2)^{-1/2}$. Those
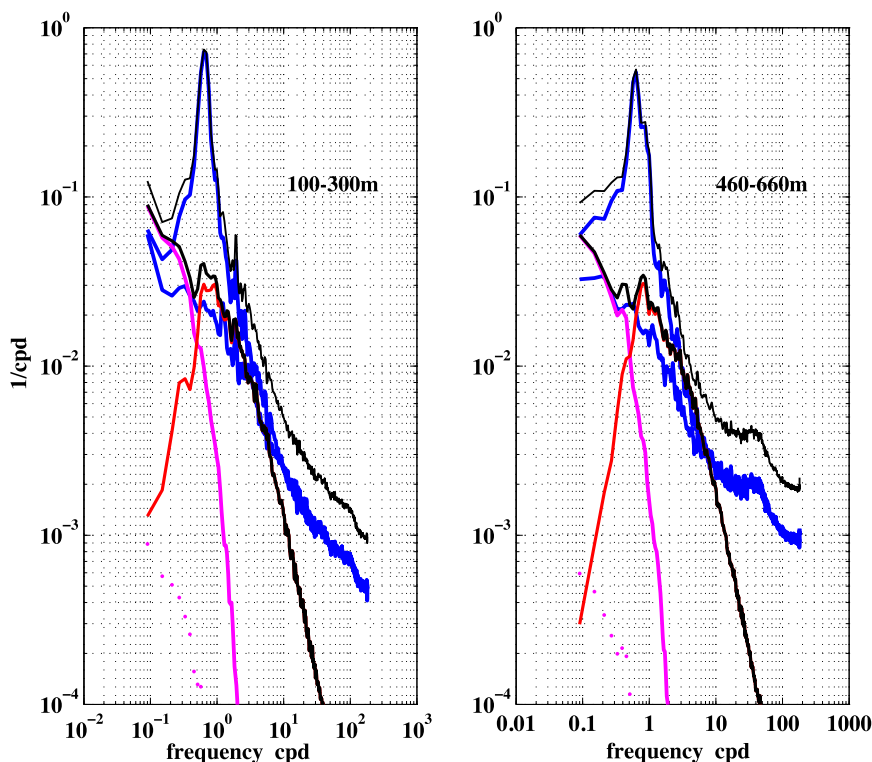
FIG. 15. Frequency spectra of $S/\overline{N}(z)$ and strain from depth ranges (left) 100–300 and (right) 460–660 m. ACy and Cy $S/\overline{N}(z)$ are given by the upper and lower blue lines. The upper black line represents their sum. The magenta and red lines represent the vortical and internal wave strain power spectra, respectively. The lower black line is their sum, the total strain spectrum. The lower magenta dotted line indicates the theoretical vortical contribution to the overall $S/\overline{N}(z)$ spectrum, assuming Br = 0.1.

who use thermocline strain to estimate deep diapycnal mixing rates (e.g., Kunze et al. 2006; Whalen et al. 2012) are, indeed, measuring primarily wave and not vortical strain. Shear-based parameterizations of mixing are primarily sensitive to local inertial activity, while strain-based estimates reflect the level of the internal wave continuum.

From the observed degree of Doppler shifting of the vortical field, an aspect ratio of order $k_H/k_z \sim 10^{-3}$, Br $\sim 10^{-1}$, is inferred. While small, these values are, if anything, upper bounds, given that rather low values of the rms advecting velocity μ were selected to fit the observed strain spectra (see Table 1). For such motions, the contribution to rms potential vorticity from vertical straining is four orders of magnitude greater than that from relative vorticity. Indeed, rms internal wave relative vorticity, as inferred from strain, is greater than vortical PV variability (Fig. 16a) and far greater than vortical relative vorticity.

Near-inertial shear exceeds anticipated vortical shear by two orders of magnitude in spectral density (Fig. 15).

The observation is that near-inertial shear is Doppler shifted across much of the internal wave band, significantly obscuring the subinertial gap in the frequency spectrum predicted by linear dynamics (e.g., Fig. 1). Yet aspect ratios for the near-inertial field are expected to be similar to those found here for the vortical field, $O(10^{-3})$ or smaller (e.g., Pinkel 2008). The reason near-inertial Doppler smearing is "so big" while vortical smearing is "so small" is that the near-inertial peak simply dominates the spectrum of internal wave and vortical shear, while the vortical strain spectrum is rather modest relative to the internal wave strain continuum. The "extent of Doppler shifting" of both fields is rather similar; this is well described by the Pinkel (2008) [Eq. (7), here] model.

While results are consistent over 20 years of observations and 40 000 CTD profiles, these eastern Pacific measurement sites have generally been selected to avoid intense mesoscale activity. The geographic variability of the submesoscale ocean requires further exploration.
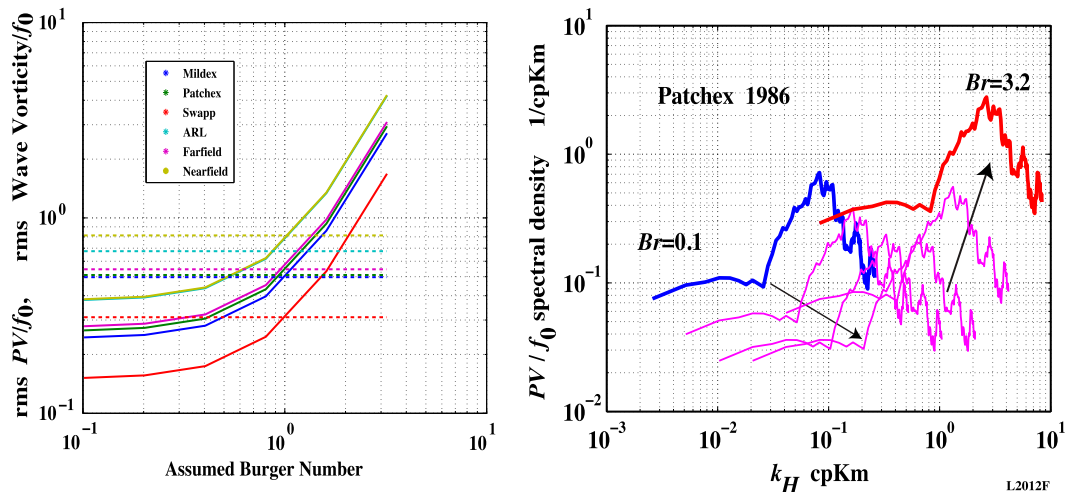
FIG. 16. Rms potential vorticity fluctuations for the (left) vortical field (solid lines) and internal wave relative vorticity (dashed lines) as inferred from strain. (right) Hypothetical horizontal wavenumber spectra of normalized potential vorticity for the 1986 Patched Experiment. The conversion from the measured vertical wavenumber spectrum (Fig. 7b) depends on the assumed aspect ratio of the vortical field. Results are plotted here for Burger numbers of 0.1, 0.2, 0.4, . . . , and 3.2. As Burger numbers increase beyond unity in both plots, the (here unmeasured) contribution of relative vorticity to the overall submesoscale PV increases rapidly.

APPENDIX A

A Brief Historical Review

By the late 1960s it was clear that internal wave dynamics governed much of the motion field at super-inertial frequencies. Vorhis (1968) presented Lagrangian measurements of vertical velocity showing a pronounced cutoff in the power spectrum of vertical displacement at the buoyancy frequency. Fofonoff (1969), using moored current meters in the Sargasso Sea, demonstrated that the relative levels of frequency spectra of horizontal velocity and vertical displacement were consistent with internal wave theory.

At small vertical scales, the picture was much less clear. The compelling dye photographs of Woods (1968), coupled with vertical profiling measurements of temperature

(e.g., Osborn and Cox 1972), revealed a very steppy, "sheet and layer"–like structure to the thermocline. While Orlanski and Bryan (1969) argued that the steps were the signature of small-scale internal waves, many scientists withheld judgment. Features of vertical scale less than 50 m became generically referred to as "fine structure."

Whatever the dynamics of this field, the fine structure was clearly advected by large-scale internal waves. This advection leads to broadband contamination of Eulerian time series, as the fine structure is translated past fixed-depth sensors. The first paper published in the *Journal of Physical Oceanography* (Phillips 1971) was devoted to modeling this effect. More sophisticated models followed by Garrett and Munk (1971), McKean (1974), Joyce and Desaubies (1977), and others.

In general, the focus was on explaining the disparity between temperature and velocity power spectra and vertical coherences. A frozen field of velocity or temperature fine structure, when vertically advected by a modeled internal wavefield, provided the contamination signal. There was an early emphasis on identifying a "frequency spectrum of the contamination," which when added to the internal wave signal would replicate the Eulerian observations.

The Garrett and Munk (1972) internal wave model considered variance at vertical scales greater than ~400 m as primarily due to internal waves (their $j_* = 10$), with smaller vertical-scale motions ascribed to fine structure of unspecified dynamics. By 1975, the GM vertical wavenumber bandwidth was extended down to 10-m scale. Virtually all of the shear and strain in the sea

was now attributed to internal waves, as opposed to none before. Compelling models of the "reversible fine structure" (Desaubies and Gregg 1981) engendered by internal wave strain were developed, and the space–time variability of dynamically interesting variables such as the Richardson number, Ri = S^2/N^2, were modeled based on internal wave scaling (e.g., Munk 1981; Desaubies and Smith 1982; Pinkel and Anderson 1997).

Still, Holloway (1983) cautioned that there are motions at fine vertical scales in the sea that are not internal waves. He suggested that small-scale quasigeostrophic motions are Doppler shifted by the ambient currents across the internal wave frequency band and contribute significantly to observed finescale shear and strain estimates. This so-called vortical/submesoscale field is associated with potential vorticity variability, in contrast to the internal wavefield, which does not induce PV fluctuations. In a determined effort, Muller (1984, 1988), Muller et al. (1988), and Lien and Muller (1992) explored the theory of the vortical mode, searched for its presence in IWEX data, and produced an integrated set of consistency relations for both vortical and internal wave motions. Muller et al. (1988) reported estimates of the vertical component of relative vorticity one to three orders of magnitude greater than predicted in the Garrett and Munk (1975) spectral model, suggesting a strong vortical signal. Vorticity estimates were obtained from a comparison of triads of current meters forming an equilateral triangle in the horizontal plane at five vertical levels in the 1972 IWEX array (Briscoe 1975). Kunze et al. (1990) subsequently argued that the spatial aliasing of this array was responsible for the large estimates of relative and potential vorticity. Subsequent contributions by Kunze et al. (1990), Kunze and Sanford (1993), and Polzin et al. (2003) are discussed in the introduction.

APPENDIX B

A Model-Based Separation of Vortical and Internal Wave Strain

It is reasonable to assume that, in an isopycnal-following frame, the vortical signal would be concentrated at frequency $\sigma = 0$, were it not for the presence of time-varying background horizontal flows. These Doppler shift the signal by an amount $\Delta\sigma = k_H V$, where V varies from realization to realization of the process. In this situation, the expected frequency spectrum of the signal is given by

$$E_m(\sigma) = E_0/k_H P_V(\sigma/k_H), \quad \text{(B1)}$$

where k_H is the horizontal wavenumber of the vortical signal, and P_V is the probability density function of the horizontal advecting velocity, V [Pinkel (2008); Eq. (7)].

For simplicity, we assume that the aspect ratio of the vortical field is the same at all vertical scales:

$$k_H/k_z = \text{Br}(f/\overline{N}). \quad \text{(B2)}$$

Then,

$$E_m(\sigma, k_z) = E_0(k_z)/[\text{Br}(f/\overline{N})k_z]P_V\{\sigma/[\text{Br}(f/\overline{N})k_z]\}, \quad \text{(B3)}$$

where $E_0(k_z)$ is the vertical wavenumber spectrum of the vortical strain. One can now match the model with the observed strain spectrum $E_m(\sigma, k_z)$ at zero frequency,

$$E_m(0, k_z) = E_0(k_z)/[\text{Br}(f/\overline{N})k_z]P_V(0), \quad \text{(B4)}$$

solve for the vortical spectrum $E_0(k_z)$, and use this relationship to specify the vortical portion of the overall strain spectrum at all observed frequencies σ. The key assumption is that the amount of internal wave variance Doppler shifted to zero frequency is small compared to the vortical contribution.

Taking Gaussian

$$P_V(V) = 1/\sqrt{2\pi\mu^2}\exp(-V^2/2\mu^2)$$
$$= 1/\sqrt{2\pi\mu^2}\exp\{-\sigma^2/2[\text{Br}(f/\overline{N})k_z\mu]^2\}, \quad \text{(B5)}$$

where μ^2 is the variance of east and north advecting velocities, (B3) is evaluated to model the vortical strain spectrum (Fig. 4c). This, when subtracted from the overall strain spectrum (Fig. 4a), provides an estimate of the internal wave strain spectrum (Fig. 4b).

To properly compare the model with the observed spectra, the model is subjected to the identical smoothing in wavenumber and frequency, as are the data-based spectral estimates. For each of the six datasets, the single tunable parameter (μBr), in conjunction with the observed strain spectrum at zero frequency $E_m(0, k_z)$, specifies the vortical model.

Not surprisingly, with the observed spectrum varying over orders of magnitude, overestimates in the simple model result in negative values for the residual "internal wave spectrum" (e.g., Fig. 4b). Rather than produce an elaborate "optimally tuned" model that minimizes obvious errors, the approach here is to maximize simplicity and note where discrepancies are found.

In early implementations of the model, it became apparent that one key idealization was significantly in error. The model sets the level of the vortical spectrum from the observed zero-frequency strain spectrum $E_m(0, k_z)$. At high wavenumbers, significant internal wave strain is Doppler shifted to zero frequency, adding to the vortical contribution. Unless this contribution is removed,
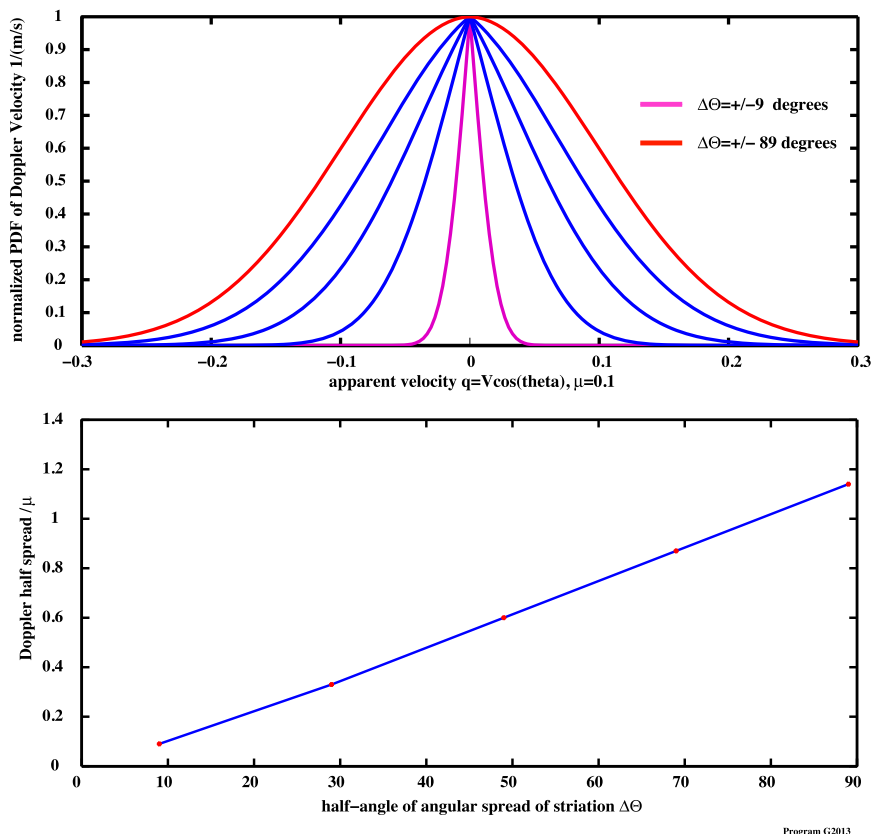
FIG. C1. (top) The PDF of apparent velocity $q = |V|\cos(\Theta)$, normalized to have maximum value unity, for angular spreads $\Delta\Theta = \pm 9°$ (magenta) to $\pm 89°$ (red). (bottom) The associated observed Doppler spread, normalized by the rms advecting velocity. For striations oriented $\pm 10°$ relative to the velocity field the magnitude of observed Doppler shifts is reduced by a factor of 10 relative to the isotropic case.

the model will overestimate the high-wavenumber vortical strain. As a simple response to this problem, the fraction $F_0 = \exp(-k_z/k_{\mathrm{Ny}})$ of $E(0, k_z)$ is attributed to the vortical field, while the remainder is considered due to the internal waves. With this reduction factor, the tendency of the model to overestimate the high-wavenumber vortical spectrum is lessened.

APPENDIX C

The Probability Density Function of Doppler Shift When the Orientation of Striations is Related to the Direction of the Advecting Velocity

We consider a situation where a signal of the form $\gamma = \gamma_0 \exp(i\overline{k}_H \cdot x)$ is advected by the random 2D velocity field $\overline{V}$ and where the *range of orientation* of $\overline{k}_H$ is restricted relative to the direction of $\overline{V}$. Specifically, we allow the direction of $\overline{k}_H$ to vary with uniform probability through the range of angles $\pm\Delta\Theta$ about $\pi/2$ relative to the direction of $\overline{V}$.

An expression for the probability density function (PDF) of Doppler shift $q' = |\overline{k}_H||\overline{V}|\cos(\Theta)$ is sought. For small $\Delta\Theta$, the striations are nearly parallel to the velocity and minimal Doppler shifting is expected. As $\Delta\Theta$ approaches $\pi/2$, the orientation of the signal relative to the advecting velocity is unconstrained, and the expression for the Doppler-shifted spectrum should approach the result of Pinkel (2008) [Eqs. (6)–(8) here and appendix B].

Assuming that $|\overline{V}|$ is Rayleigh distributed, the joint PDF of $|\overline{V}|$ and Θ is

$$P(V, \Theta) = \begin{cases} 1/(2\mu^2\Delta\Theta)V e^{-(V^2/2\mu^2)} & \pi/2 - \Delta\Theta < \Theta < \pi/2 + \Delta\Theta \\ 0 & \text{elsewhere} \end{cases} \tag{C1}$$

The associated PDF of $|\overline{V}|$ and $z = \cos(\Theta)$ is

$$P(V, z) = \begin{cases} 1/(2\mu^2 \Delta\Theta \sqrt{1 - z^2})Ve^{-(V^2/2\mu^2)} & \cos(\pi/2 + \Delta\Theta) < z < \cos(\pi/2 - \Delta\Theta) \\ 0 & \text{elsewhere} \end{cases} \quad \text{(C2)}$$

The PDF of the product $q = q'/|k_H| = |\overline{V}| \cos(\Theta) = Vz$ is found by writing (C2) in terms of q and V and subsequently integrating over V:

$$P(V, q) = 1/(2\mu^2 \Delta\Theta \sqrt{1 - q^2/V^2})e^{-(V^2/2\mu^2)},$$
$$|q| < \cos(\pi/2 - \Delta\Theta). \quad \text{(C3)}$$

For $q > 0$, positive Doppler shifts, the integral takes the form

$$P_q(q) = 1/(2\mu^2 \Delta\Theta) \int_{V = q/\cos(\pi/2 - \Delta\Theta)}^{\infty} V/\sqrt{V^2 - q^2} e^{-(V^2/2\mu^2)} dV. \quad \text{(C4)}$$

Substituting $\alpha = \sqrt{V^2 - q^2}$, one obtains the integral

$$P_q(q) = 1/(2\mu^2 \Delta\Theta)e^{-(q^2/2\mu^2)} \int_{q\tan(\pi/2 - \Delta\Theta)}^{\infty} e^{-(\alpha^2/2\mu^2)} d\alpha, \quad \text{(C5)}$$

yielding a PDF for Doppler shift of the form

$$P_q(q) = \sqrt{\pi/2}/(2\mu\Delta\Theta)e^{-(q^2/2\mu^2)}$$
$$\times [1 - \text{erf}(q\cot(\Delta\Theta)/\sqrt{2}\mu)]. \quad \text{(C6)}$$

The units of P_q are inverse velocity. The associated PDF $P_{q'} = 1/k_H P_q(k_H q)$ gives the Doppler spectrum in units of frequency. Clearly, as $\Delta\Theta$ approaches $\pi/2$, $\cot(\Delta\Theta)$ vanishes and the Gaussian form of the spectrum is recovered. However, for striations more tightly constrained along the direction of flow, the PDF is much narrower than a Gaussian (Fig. C1).

REFERENCES

Alford, M., and R. Pinkel, 2001: Observations of overturning in the thermocline: The context of ocean mixing. *J. Phys. Oceanogr.,* **31,** 805–832, doi:10.1175/1520-0485(2000)030<0805:OOOITT>2.0.CO;2.

Anderson, S. A., 1992: Shear, strain, and thermocline vertical fine structure in the upper ocean. Ph.D. thesis, University of California, San Diego, 173 pp.

Briscoe, M. G., 1975: Preliminary results from the tri-moored Internal Wave Experiment (IWEX). *J. Geophys. Res.,* **80,** 3872–3884, doi:10.1029/JC080i027p03872.

Desaubies, Y. J. F., and M. C. Gregg, 1981: Reversible and irreversible finestructure. *J. Phys. Oceanogr.,* **11,** 541–556, doi:10.1175/1520-0485(1981)011<0541:RAIF>2.0.CO;2.

——, and W. K. Smith, 1982: Statistics of Richardson number and instability in oceanic internal waves. *J. Phys. Oceanogr.,* **12,** 1245–1259, doi:10.1175/1520-0485(1982)012<1245:SORNAI>2.0.CO;2.

Ertel, H., 1942: Ein neuer hydrodynamischer Wirbelsatz. *Meteor. Z.,* **59,** 277–281.

Fofonoff, N. P., 1969: Spectral characteristics of internal waves in the ocean. *Deep-Sea Res.,* **16** (Suppl.), 58–71.

Garrett, C. J. R., and W. H. Munk, 1971: Internal wave spectra in the presence of finestructure. *J. Phys. Oceanogr.,* **1,** 196–202, doi:10.1175/1520-0485(1971)001<0196:IWSITP>2.0.CO;2.

——, and ——, 1972: Space-time scales of internal waves. *Geophys. Fluid Dyn.,* **3,** 225–264, doi:10.1080/03091927208236082.

——, and ——, 1975: Space-time scales of internal waves: A progress report. *J. Geophys. Res.,* **80,** 291–297, doi:10.1029/JC080i003p00291.

Gerkema, T., L. R. M. Maas, and H. van Haren, 2013: A note on the role of mean flows in Doppler shifted frequencies. *J. Phys. Oceanogr.,* **43,** 432–441, doi:10.1175/JPO-D-12-090.1.

Holloway, G., 1983: A conjecture relating oceanic internal waves and small-scale processes. *Atmos.–Ocean,* **21,** 107–122, doi:10.1080/07055900.1983.9649159.

Joyce, T. M., and Y. J. F. Desaubies, 1977: Discrimination between internal waves and temperature finestructure. *J. Phys. Oceanogr.,* **7,** 22–32, doi:10.1175/1520-0485(1977)007<0022:DBIWAT>2.0.CO;2.

Kunze, E., and T. B. Sanford, 1993: Submesoscale dynamics near a seamount. Part I: Measurements of Ertel vorticity. *J. Phys. Oceanogr.,* **23,** 2567–2588, doi:10.1175/1520-0485(1993)023<2567:SDNASP>2.0.CO;2.

——, M. G. Briscoe, and A. J. Williams, 1990: Interpreting shear and strain finestructure from a neutrally buoyant float. *J. Geophys. Res.,* **95,** 18 111–18 125, doi:10.1029/JC095iC10p18111.

——, E. Firing, J. M. Hummon, T. K. Chereskin, and A. M. Thurnherr, 2006: Global abyssal mixing inferred from lowered ADCP shear and CTD strain profiles. *J. Phys. Oceanogr.,* **36,** 1553–1576, doi:10.1175/JPO2926.1.

Leaman, K. D., and T. B. Sanford, 1975: Vertical energy propagation of inertial waves: A vector spectral analysis of velocity profiles. *J. Geophys. Res.,* **80,** 1975–1978, doi:10.1029/JC080i015p01975.

Lien, R.-C., and P. Muller, 1992: Consistency relations for gravity and vortical modes in the ocean. *Deep-Sea Res.,* **39,** 1595–1612, doi:10.1016/0198-0149(92)90050-4.

Marmorino, G. O., L. J. Rosenblum, and C. L. Trump, 1987: Finescale temperature variability: The influence of near-inertial

waves. *J. Geophys. Res.,* **92,** 13 049–13 062, doi:10.1029/JC092iC12p13049.

McKean, R. S., 1974: Interpretation of internal wave measurements in the presence of fine structure. *J. Phys. Oceanogr.,* **4,** 200–213, doi:10.1175/1520-0485(1974)004<0200:IOIWMI>2.0.CO;2.

Muller, P., 1984: Small-scale vortical motions. *Internal Gravity Waves and Small-Scale Turbulence: Proc. 'Aha Huliko'a Hawaiian Winter Workshop,* Honolulu, HI, University of Hawai'i at Mānoa, 249–262.

——, 1988: Vortical motions. *Small-Scale Turbulence and Mixing in the Ocean,* J. C. J. Nihoul and B. M. Jamart, Eds., Elsevier, 285–301.

——, R.-C. Lein, and R. G. Williams, 1988: Estimates of potential vorticity at small scales in the ocean. *J. Phys. Oceanogr.,* **18,** 401–416, doi:10.1175/1520-0485(1988)018<0401:EOPVAS>2.0.CO;2.

Munk, W. H., 1981: Internal waves and small-scale processes. *Evolution of Physical Oceanography,* B. A. Warren and C. Wunsch, Eds., The MIT Press, 264–291.

Orlanski, I., and K. Bryan, 1969: Formation of the thermocline step structure by large-amplitude internal gravity waves. *J. Geophys. Res.,* **74,** 6975–6983, doi:10.1029/JC074i028p06975.

Osborn, T. R., and C. S. Cox, 1972: Oceanic fine structure. *Geophys. Fluid Dyn.,* **3,** 321–345, doi:10.1080/03091927208236085.

Phillips, O. M., 1971: On spectra measured in an undulating layered medium. *J. Phys. Oceanogr.,* **1,** 1–6, doi:10.1175/1520-0485(1971)001<0001:OSMIAU>2.0.CO;2.

Pinkel, R., 1975: Upper ocean internal wave observations from *FLIP. J. Geophys. Res.,* **80,** 3892–3910, doi:10.1029/JC080i027p03892.

——, 1979: Observations of strongly nonlinear internal motion in the open sea using a range-gated Doppler sonar. *J. Phys. Oceanogr.,* **9,** 675–686, doi:10.1175/1520-0485(1979)009<0675:OOSNIM>2.0.CO;2.

——, 1981: On the use of Doppler sonar for internal wave measurements. *Deep-Sea Res.,* **28A,** 269–289, doi:10.1016/0198-0149(81)90067-4.

——, 1983: Doppler sonar observations of internal waves: Wavefield structure. *J. Phys. Oceanogr.,* **13,** 804–815, doi:10.1175/1520-0485(1983)013<0804:DSOOIW>2.0.CO;2.

——, 2008: Advection, phase distortion, and the frequency spectrum of finescale fields in the sea. *J. Phys. Oceanogr.,* **38,** 291–313, doi:10.1175/2007JPO3559.1.

——, and S. A. Anderson, 1997: Shear, strain, and Richardson number variations in the thermocline. Part I: Statistical description. *J. Phys. Oceanogr.,* **27,** 264–281, doi:10.1175/1520-0485(1997)027<0264:SSARNV>2.0.CO;2.

Polzin, K. L., E. Kunze, J. M. Toole, and R. W. Schmitt, 2003: The partition of finescale energy into internal waves and sub-inertial motions. *J. Phys. Oceanogr.,* **33,** 234–248, doi:10.1175/1520-0485(2003)033<0234:TPOFEI>2.0.CO;2.

Rainville, L., and R. Pinkel, 2006: Propagation of low-mode internal waves through the ocean. *J. Phys. Oceanogr.,* **36,** 1220–1236, doi:10.1175/JPO2889.1.

Sherman, J. T., and R. Pinkel, 1991: Estimates of the vertical wavenumber–frequency spectra of vertical shear and strain. *J. Phys. Oceanogr.,* **21,** 292–303, doi:10.1175/1520-0485(1991)021<0292:EOTVWS>2.0.CO;2.

Sun, O. M., and R. Pinkel, 2013: Subharmonic energy transfer from the semidiurnal tide to near-diurnal motions at Kaena Ridge, Hawaii. *J. Phys. Oceanogr.,* **43,** 766–789, doi:10.1175/JPO-D-12-0141.1.

Vorhis, A. D., 1968: Measurement of vertical motion and the partition of energy in New England slope water. *Deep-Sea Res. Oceanogr. Abstr.,* **15,** 599–609, doi:10.1016/0011-7471(68)90065-X.

Whalen, C. B., L. D. Talley, and J. A. MacKinnon, 2012: Spatial and temporal variability of global ocean mixing inferred from Argo profiles. *Geophys. Res. Lett.,* **39,** L18612, doi:10.1029/2012GL053196.

Woods, J. D., 1968: Wave-induced shear instability in the summer thermocline. *J. Fluid Mech.,* **32,** 791–800, doi:10.1017/S0022112068001035.